



Design, Synthesis, Molecular Docking, Antimicrobial and Anticancer Activity of Novel Quinazoline Amino Acid Hybrids



CrossMark

Heba A. El-Sayed¹, Hanan Afifi², Abdel-Aziz Ebead³, Ibrahim M. Nagy^{4*}, Abdel-Rahman A. El-Attar¹, Adel A.-H. Abdel-Rahman^{1*}

¹ Chemistry Department, Faculty of Science, Menoufia University, Shebin El-Koam, 32511 Egypt

² Faculty of Industrial Education, Beni Suef University, Beni Suef, 62512 Egypt

³ Chemistry Department, Faculty of Science, Arish University, Arish, 45511 Egypt

⁴ Medicinal Chemistry Department, Menoufia University, Shebin El-Koam, 32511 Egypt

Abstract

A novel series of quinazoline–amino acid hybrids has been synthesized through a multistep synthetic pathway. The synthesized compounds include ester derivatives (**3**, **4**), hydrazide derivatives (**5**, **6**, **13**, **17**), dipeptides (**14–16**), and tripeptides (**18–20**) of quinazoline. Their structures were confirmed via IR, ¹H-NMR, and ¹³C-NMR spectroscopy, along with elemental analysis. The antimicrobial evaluation revealed that all compounds exhibited moderate to strong activity, with compounds **4–6**, **15**, **16**, and **18–20** displaying the most potent antibacterial and antifungal properties. Specifically, compound **6** demonstrated (39 mm, MIC = 8 μM, IC₅₀ = 7 μM) inhibition zone against *Bacillus subtilis* (36 mm, MIC = 11 μM, IC₅₀ = 9 μM) inhibition against *E. coli*, and compound **4** showed strong activity against *Escherichia coli* with an inhibition of (33 mm, MIC = 13 μM, IC₅₀ = 11 μM). The antifungal activity was also notable, with compound **16** showing (13 mm, MIC = 35 μM, IC₅₀ = 28 μM) inhibition against *Candida albicans*. Furthermore, molecular docking studies highlighted their strong binding affinities to key microbial targets, with compound **19** exhibiting the top docking score (ΔG = −8.46 kcal/mol), compared to erlotinib (ΔG = −8.51 kcal/mol). In addition, the anticancer potential of the synthesized compounds was assessed in vitro against MCF7 breast cancer cells using the SRB assay. Compound **15** displayed significant cytotoxicity with an IC₅₀ value of 3.40 ± 0.13 μg/mL, demonstrating pharmacological performance comparable to doxorubicin (IC₅₀ = 2.97 ± 0.12 μg/mL). These findings underscore the promising therapeutic applications of quinazoline–amino acid hybrids, warranting further investigation into their biological mechanisms and clinical relevance.

Keywords: Quinazoline, synthesis, hydrazide, peptides, antimicrobial, anticancer.

1. Introduction

Cancer is one of the most widespread and High-risk diseases globally, ranking as the second primary cause of mortality. It is marked by uncontrolled cell proliferation and impaired cell death, leading to abnormal tissue growth [1]. Various treatment approaches, such as chemotherapy, surgery, radiotherapy, and immunotherapy, have been developed to combat cancer. However, the search for highly effective chemotherapy drugs with minimal side effects remains a priority [2]. Gaining deeper insights into the molecular and cellular mechanisms underlying cancer has significantly advanced therapeutic strategies. Many types of cancer progress due to abnormalities in key cellular signaling pathways [3]. These are often driven by the dysregulated activation of critical signaling proteins, which include platelet-derived growth factor receptors (PDGFRs), receptor tyrosine kinases (RTKs), epidermal growth factor receptors (EGFRs), and vascular endothelial growth factor receptors (VEGFRs). These receptors are critically involved in controlling essential cellular functions such as proliferation, resistance to apoptosis, motility, and angiogenesis (the formation of new blood vessels) [4].

In cancer, their over activation or mutation can cause unrestrained cell growth and tumor development. As a result, targeting these receptors has become a key therapeutic strategy in cancer treatment. By inhibiting the signaling pathways mediated by these receptors, it is possible to disrupt the tumor's ability to grow and metastasize, offering a promising avenue for the development of targeted therapies that are more specific and potentially less toxic than traditional chemotherapy [5]. Quinazolines have garnered significant attention due to their potency and selectivity in chemotherapy [6, 7]. Several FDA-approved anticancer drugs, including erlotinib, lapatinib, and gefitinib, feature a quinazoline core and function as EGFR inhibitors (**I**) [8–15]. Additionally, quinazoline-based compounds, for example, WHI-P180 (**II**) and **III** exhibit strong anticancer properties by inhibiting both EGFR and VEGFR kinases [16, 17] (Figure 1).

Historically, quinazoline derivatives have played a pivotal role in medicinal chemistry, dating back to the early 20th century when their antibacterial and antimalarial activities were first explored. Over the decades, extensive research has led to the development of quinazoline-based drugs not only for cancer but also for cardiovascular, neurological, and inflammatory

*Corresponding author e-mail: ibrahimnagy325@gmail.com; adelnassar63@yahoo.com; (Ibrahim M. Nagy) (Adel A.-H. Abdel-Rahman).

Received date 06 April 2025; Revised date 16 May 2025; Accepted date 10 June 2025

DOI: 10.21608/ejchem.2025.373139.11550

©2025 National Information and Documentation Center (NIDOC)

disorders. Notably, the structural versatility and ability to modulate multiple biological targets have made quinazolines a privileged scaffold in drug design. Key studies have demonstrated their efficacy as kinase inhibitors (e.g., EGFR, VEGFR, PDGFR), tubulin polymerization inhibitors, and DNA intercalators [18,19]. For instance, Ward *et al.* reported the synthesis of quinazoline derivatives with dual EGFR/VEGFR inhibitory activity, which showed significant tumor regression in preclinical models [20]. These findings have established quinazolines as a cornerstone in the design of modern targeted therapies [21].

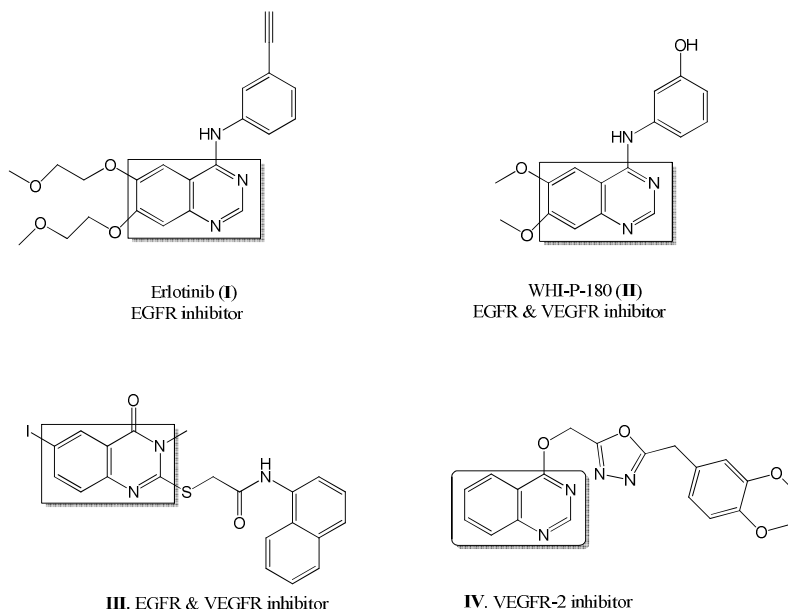


Figure 1: Reported quinazoline as EGFR and VEGFR-2 inhibitors

In addition to their anticancer properties, organic compounds—particularly heterocyclic structures like quinazolines—have long been investigated for their antimicrobial potential. These compounds can interfere with vital microbial processes such as cell wall synthesis, DNA replication, and protein synthesis. Substituted quinazolines, triazoles, and amino acid conjugates have shown promising antibacterial and antifungal activities in both clinical and experimental settings. Their structural flexibility allows for functional group modifications, enhancing selectivity and potency against a wide spectrum of pathogens [22–26]. Therefore, the design of multifunctional organic scaffolds holds great promise for developing dual-purpose agents with both antimicrobial and anticancer effects.

Conversely, amino acid conjugates are pharmacologically significant because they can improve aqueous solubility, enhance membrane permeability, and facilitate active transport through amino acid transporters, thereby increasing the bioavailability and cellular uptake of the drug molecules [27]. Consequently, quinazoline derivatives linked to amino acids are promising candidates, as the quinazoline structure enables their application as fluorescent probes [28, 29]. Furthermore, numerous amino acids incorporating heterocyclic groups have been identified as potent antitumor agents [30–32].

In this study, peptide linkages were deliberately incorporated into the quinazoline scaffold to combine the anticancer potential of quinazolines with the pharmacokinetic advantages conferred by amino acids. The underlying hypothesis is that such conjugation could enhance drug selectivity, improve cellular internalization, and potentially exploit specific amino acid transporters overexpressed in cancer cells. Moreover, the use of diverse amino acids introduces variability in hydrophobicity, steric properties, and hydrogen-bonding capabilities, which may significantly influence receptor binding affinity and antimicrobial activity. These strategic modifications aim to optimize both anticancer and antimicrobial profiles by leveraging the synergistic effects of the quinazoline core and bioactive peptide moieties.

Building on the previously established synthetic strategies for developing novel target compounds [33–40], this work aims to contribute to the Development and production of new active lead candidates. Specifically, the goal is to explore the design, synthesis, molecular docking, and assessment of the antimicrobial and antitumor activity of these quinazoline derivatives and their peptide analogues. To confirm the chemical structures of these compounds, we utilized infrared (IR), mass, nuclear magnetic resonance ^1H - and ^{13}C -NMR spectroscopy.

2. Material and Methods

2.1. Chemistry

In this study, all chemicals were sourced from reputable commercial suppliers, including Sigma-Aldrich, Fluka, Acros, BDH, and Merck. These chemicals were of analytical grade, ensuring their high purity, and were used directly without any additional purification steps. For the solvents used in the reactions, they were distilled according to standard laboratory procedures before use, which involved drying and removing any impurities to maintain consistency and quality in the

experimental results. The purity of the solvents was critical to ensure that the reactions proceeded efficiently and without contamination. To monitor the development of chemical reactions, thin-layer chromatography (TLC) was employed. This technique involved the employ of Silica gel-coated plates as the stationary phase, with the reaction mixtures being spotted on the plates and allowed to travel in a solvent. Ultraviolet (UV) light at 254 nm was used solely for spot visualization on thin-layer chromatography (TLC) plates. This technique served as a straightforward and effective method for monitoring reaction progress and detecting unreacted starting materials. The TLC method provided a simple, yet effective, means of evaluating the completeness of reactions and determining the presence of any unreacted starting materials. Melting point measurements were carried out *via* a Thermo Fisher Scientific instrument. The values were recorded directly from the instrument without any correction, as it provided accurate readings of the physical properties of the compounds, which were essential for confirming their identity and purity. The determination of the melting point is a crucial parameter in compound characterization, providing insight into the purity and crystallinity of the synthesized material. For the identification and confirmation of functional groups inside the compounds, Fourier-transform infrared (FT-IR) spectroscopy was used. The functional groups present in the compounds were analyzed using a Bruker Tensor 27 FT-IR spectrophotometer, which provided detailed information about the types of bonds and functional groups through their characteristic absorption bands. This spectral technique allowed for the identification of key functional groups such as amides, esters, and aromatic rings, further verifying the successful synthesis of the compounds. To fully characterize the molecular structure of the compounds, ^1H -NMR spectroscopy was employed. A Bruker spectrometer at 100 MHz for ^{13}C -NMR and 400 MHz for ^1H -NMR frequencies was used to obtain high-resolution spectra. In ^1H -NMR, the chemical shifts (δ) were calculated in part per million (ppm), with tetramethylsilane (TMS) as the internal standard. Similarly, ^{13}C -NMR spectra were recorded to provide information on the carbon environments in the molecules. The NMR data were essential for elucidating the structural details, including the placement of hydrogen and carbon atoms in the synthesized compounds. Dimethyl sulfoxide ($\text{DMSO}-d_6$) was used as the solvent to dissolve the compounds at a concentration of 1×10^{-6} M, and the spectra were measured to provide insight into the electronic transitions within the molecules. This analysis helped in confirming the chemical nature of the compounds, particularly for those with conjugated systems that show distinct absorbance characteristics. Mass spectrometry was employed to report the molecular weights and fragmentation patterns of the synthesized compounds. A Shimadzu QP 5050 Ex spectrometer was employed for this purpose, providing accurate mass to charge ratio (m/z) for the molecular and fragment ions. The mass spectra helped in confirming the molecular formulas of the compounds and identifying any possible degradation products, ensuring that the compounds were correctly synthesized.

Finally, elemental analysis was employed using a PerkinElmer elemental analyzer at the Faculty of Applied Science, Tokyo University, Japan. The elemental analysis was crucial for verifying the molecular composition of the compounds. The experimental values for the carbon, hydrogen, and nitrogen content were found to deviate by no more than $\pm 0.4\%$ from the theoretical calculations, which confirmed the high purity and accurate synthesis of the compounds. This thorough analysis confirmed that all the synthesized compounds were of the expected purity and identity, suitable for further biological testing.

2.1.1. Synthesis of ethyl 2-(3-methyl-4-oxo-3,4-dihydroquinazolin-2-ylthio)acetate (3) and ethyl 2-(6-chloro-3-methyl-4-oxo-3,4-dihydroquinazolin-2-ylthio)acetate (4) [41, 42]

To synthesize compound **3**, the starting materials (10 mmol) was mixed with ethyl chloroacetate (10 mmol, 1.22 mL) and anhydrous potassium carbonate (10 mmol, 1.38 g) in distilled acetone. This reaction was then refluxed for approximately 12 h to facilitate the desired chemical transformation. After the reaction time, the reaction was filtered off on hot to eliminate any solid impurities that may have formed during the reaction. The filtrate was then added onto cold ice-water, leading to the precipitation of the product. To ensure thorough removal of any residual unreacted materials or by-products, the resulting solid was washed with water. The product was then purified by recrystallization from ethanol, resulting in the isolation of compound **3** in a yield of 90%. The physical properties of the synthesized compound were characterized, revealing a melting point ranging from 179–181°C. The infrared (IR) spectrum (KBr, cm^{-1}) displayed the following characteristic peaks: 3069 cm^{-1} for aromatic CH stretching, 2979 cm^{-1} for aliphatic CH stretching, a strong absorption at 1735 cm^{-1} indicates the ester carbonyl ($\text{C}=\text{O}$) group and 1612 cm^{-1} indicative of $\text{C}=\text{C}$ stretching. ^1H -NMR spectrum (400 MHz, $\text{DMSO}-d_6$) showed the following signals δ (ppm): 1.28 (t, 3H, $J = 6.1$ Hz, $\text{CH}_3\text{CH}_2\text{O}$), 3.44 (s, 3H, NCH_3), 4.02 (s, 2H, SCH_2), 4.13 (q, 2H, $J = 6.1$ Hz, $\text{CH}_3\text{CH}_2\text{O}$), 7.60–7.89 (m, 4H, Ar-H). Elemental analysis for compound **3** ($\text{C}_{13}\text{H}_{14}\text{N}_2\text{O}_3\text{S}$, molecular weight 278.34) was performed, yielding the following results: the calculated values were C 56.12%, H 5.08%, N 10.08%, and the experimental values were C 56.10%, H 4.95%, N 9.88%, which are in close agreement, confirming the compound's composition and purity. To synthesize compound **4**, the reaction mixture was prepared similarly to the procedure for compound **3**, with slight variations in the specific reagents and conditions used. The desired product was in 85% yield, with a melting point ranging from 193–195°C. The infrared (IR) spectrum (KBr, cm^{-1}) displayed key absorption bands indicative of functional groups in the structure: 3077 cm^{-1} , corresponding to the aromatic C-H stretching, a band at 2982 cm^{-1} for aliphatic C-H stretching, a sharp absorption at 1714 cm^{-1} , which is typical of ester carbonyl ($\text{C}=\text{O}$) stretching, and a peak at 1607 cm^{-1} , suggesting $\text{C}=\text{C}$ stretching, further confirming the presence of the aromatic ring in the structure. ^1H -NMR spectrum (400 MHz, $\text{DMSO}-d_6$) showed the following signals δ (ppm): 1.29 (t, 3H, $J = 6.1$ Hz, $\text{CH}_3\text{CH}_2\text{O}$), 3.40 (s, 3H, NCH_3), 4.07 (s, 2H, SCH_2), 4.15 (q, 2H, $J = 6.1$ Hz, $\text{CH}_3\text{CH}_2\text{O}$), 7.40–7.85 (m, 3H, Ar-H). Elemental analysis for $\text{C}_{13}\text{H}_{13}\text{ClN}_2\text{O}_3\text{S}$ (312.77) was also carried out, with the calculated values of C 49.93%, H 4.19%, N 8.96% and experimental values of C 49.80%, H 4.06%, N 8.79%, which confirmed the purity and correct elemental composition of the compound.

2.1.2. General procedure for synthesis of hydrazide derivatives 5, 6, 13 and 17.

A reaction containing compounds **3**, **4**, **7**, and/or **14** (10 mmol each) was prepared by dissolving them in 20 mL of absolute ethanol. Hydrazine hydrate (99%, 10 mmol) was added. The mixture was refluxed for 5–6 h to allow the reaction to proceed. After completion, excess ethanol was evaporated under reduced pressure, resulting in a precipitate. The product was filtered and purified through recrystallization from ethanol. The resulting compounds, **5**, **6**, **13**, and **17**, were obtained in good yields.

2.1.3. 2-(3-Methyl-4-oxo-3,4-dihydroquinazolin-2-ylthio)acetohydrazide (**5**)

The synthesis of the compound yielded needle-like crystals with a melting point between 200–202 °C and an excellent yield of 93%. The infrared (IR) spectrum (KBr, cm^{-1}) showed the following significant absorption bands: 3423 cm^{-1} and 3327 cm^{-1} corresponding to the N-H stretch for the amine (NH_2) and amide (NH) groups, respectively. The peak at 3077 cm^{-1} indicated aromatic C-H stretching, while the absorption at 2977 cm^{-1} corresponded to aliphatic C-H stretching. A strong peak at 1670 cm^{-1} suggested an amide carbonyl (C=O) group, and the band at 1608 cm^{-1} was indicative of C=C stretching from the aromatic ring. 1505 cm^{-1} was observed, representing C-N stretching, which confirmed the presence of a nitrogen-containing group in the compound. The elemental analysis was performed for the compound with the molecular formula $\text{C}_{11}\text{H}_{12}\text{N}_4\text{O}_2\text{S}$ (molecular weight = 264.30). The theoretical values were C 49.97%, H 4.59%, N 21.21%, while the experimental results were C 49.77%, H 4.45%, N 21.09%, indicating that the synthesized compound closely matched the expected composition, confirming its purity and identity.

2.1.4. 2-(6-Chloro-3-methyl-4-oxo-3,4-dihydroquinazolin-2-ylthio)acetohydrazide (**6**)

The synthesized compound is a pale yellow powder with a melting point ranging from 238–240 °C and a high yield of 90%. The infrared (IR) spectrum (KBr, cm^{-1}) exhibited the following significant peaks: 3421 cm^{-1} and 3325 cm^{-1} , for the stretching vibrations of the amine (NH_2) and amide (NH) groups, respectively. The absorption at 3061 cm^{-1} was attributed to aromatic C-H stretching, while the peak at 2970 cm^{-1} indicated aliphatic C-H stretching. The 1685 cm^{-1} band was associated with the carbonyl (C=O) stretching of the amide group, and the 1600 cm^{-1} band confirmed the presence of C=C stretching, indicative of the aromatic ring. The peak at 1500 cm^{-1} was attributed to C-N stretching, suggesting a nitrogen-containing structure. The elemental analysis for $\text{C}_{11}\text{H}_{11}\text{ClN}_4\text{O}_2\text{S}$ (molecular weight = 298.75). Theoretical values were C 44.22%, H 3.71%, N 18.75%, experimental results were C 44.08%, H 3.65%, N 18.55%, which are in agreement with the calculated values, further confirming the purity and structure of the compound.

2.1.5. N-(2-Hydrazinyl-2-oxoethyl)-2-(3-methyl-4-oxo-3,4-dihydroquinazolin-2-ylthio)acetamide (**13**)

The synthesized compound is a yellow crystal with a melting point ranging from 182–184 °C and a yield of 87%. The compound's structure was characterized using spectroscopic and elemental analysis techniques. The infrared (IR) spectrum (KBr, cm^{-1}) displayed the following characteristic peaks: 3730 cm^{-1} for the amine (NH_2) stretching, 3287 cm^{-1} for the amide (NH) stretch, and 3050 cm^{-1} for the aromatic C-H stretching vibrations. The absorption at 2915 cm^{-1} is attributed to aliphatic C-H stretching, while the peak at 1662 cm^{-1} for the carbonyl (C=O) stretching of the amide group. The 1610 cm^{-1} band suggests the presence of conjugated C=C double bonds in the aromatic system, and the 1545 cm^{-1} band is indicative of C-N stretching, confirming the nitrogen-containing structure. Elemental analysis for $\text{C}_{13}\text{H}_{15}\text{N}_5\text{O}_3\text{S}$ (molecular weight = 321.36) showed a close match between the calculated and experimental values: calcd % C 48.59, H 4.70, N 21.8 and found % C 48.45, H 4.49, N 21.59. These results further validate the structure and purity of the compound.

2.1.6. N-(2-Hydrazinyl-2-oxoethyl)-2-[2-(3-methyl-4-oxo-3,4-dihydroquinazolin-2-ylthio)acetamido]acetamide (**17**)

The synthesized compound appears as yellowish crystals with a melting point of 168–170 °C and a yield of 90%. In the infrared (IR) spectrum (KBr, cm^{-1}), the following notable absorption peaks were observed: 3830 cm^{-1} and 3752 cm^{-1} , indicative of amine (NH_2) and amide (NH) stretches, respectively. The peak at 3080 cm^{-1} for the aromatic C-H stretching vibrations, while 2920 cm^{-1} reflects aliphatic C-H stretching. The 1665 cm^{-1} band is associated with the carbonyl stretch (C=O) of the amide group, and the 1609 cm^{-1} absorption suggests the presence of conjugated C=C double bonds in the aromatic ring. The 1551 cm^{-1} peak is typical of C-N stretching, reinforcing the nitrogen in the compound. The elemental analysis for $\text{C}_{15}\text{H}_{18}\text{N}_6\text{O}_4\text{S}$ (molecular weight = 378.41) showed the following: the calculated values are C 47.61, H 4.79, and N 22.20, while the found values were C 47.43, H 4.53, and N 21.99, demonstrating a close agreement and confirming the compound's molecular composition and purity.

2.1.7. General procedure for synthesis of methyl 2-[2-(3-methyl-4-oxo-3,4-dihydroquinazolin-2-ylthio)acetamido]bearing amino acid esters **7-12**, **14-16** and **18-20**.

A solution containing hydrazides **5**, **6**, **13**, and **17** (4 mmol of each) was prepared by mixing them with a solvent mixture of acetic acid (30 mL), 1N HCl (15 mL), and water (125 mL). The mixture was then cooled to –5 °C by placing it in an ice bath to ensure the reaction occurred at a low temperature. To this cooled solution, a freshly prepared sodium nitrite solution (4.35 g, 63 mmol) in 15 mL of cold water was added dropwise while maintaining continuous stirring to promote uniform mixing. The reaction proceeded at –5 °C for 15 min., during which yellow azide syrup formed. After this, the syrup was extracted with chilled ethyl acetate (150 mL) to separate the organic azide. This organic phase was subsequently washed sequentially with 3% sodium bicarbonate solution (150 mL) to neutralize any remaining acidic components and then with water (150 mL) to remove any aqueous impurities. After washing, anhydrous sodium sulfate was used to remove moisture from the solution. In a separate step, the amino acid methyl ester hydrochloride (4.5 mmol) was dissolved in 100 mL of ethyl acetate, and triethylamine (1.0 mL) was added. The resulting reaction was stirred at 0 °C for 20 min. to dissolution and activation of the amino acid ester. After the stirring period, the solution was filtered to remove any solid impurities. The filtrate, which now

contained the amino acid ester, was combined with the previously prepared azide solution. The reaction was kept at -5°C for 12 h, allowing the coupling to take place at a low temperature to prevent any unwanted decomposition of the azide. After 12 h at low temperature, the reaction proceeded to come to room temperature and was kept under these conditions for another 12 h. Once the reaction was finished, the mixture was subjected to a series of washes with 0.5N HCl (150 mL) to remove any unreacted basic components, followed by a wash with 3% sodium bicarbonate solution (150 mL) to neutralize any residual acidic species, and finally washed with water (150 mL) to remove any remaining aqueous contaminants. The solution was then dried over sodium sulfate to remove excess moisture. Once dried, the filtrate was concentrated to remove ethyl acetate. The resulting residue was purified on silica gel column, using petroleum ether and ethyl acetate in a 5:1 ratio as a mobile phase. This purification method resulted in the isolation of the final compounds **7–12**, **14–16**, and **18–20** in good yields.

2.1.8. Methyl 2-[2-(3-methyl-4-oxo-3,4-dihydroquinazolin-2-ylthio)acetamido]acetate (**7**)

The synthesized compound was obtained as clear white crystals with a melting point ranging from $172\text{--}174^{\circ}\text{C}$, yield 86%. The IR spectrum absorption bands: 3370 cm^{-1} for NH stretch, 3074 cm^{-1} for aromatic CH, 2921 cm^{-1} for aliphatic CH, 1729 cm^{-1} for C=O ester, 1672 cm^{-1} for C=O amide, 1611 cm^{-1} for C=C, and 1505 cm^{-1} for C–N. The $^1\text{H-NMR}$ (400 MHz; DMSO- d_6) showed the following signals δ (ppm): 3.41 (s, 3H, NCH₃), 3.64 (s, 3H, OCH₃), 3.90 (s, 2H, SCH₂), 4.10 (s, 2H, CH₂NH), 7.60–7.70 (m, 2H, Ar-H), 7.80–8.00 (m, 2H, Ar-H), 8.06 (brs, 1H, NH, D₂O exchangeable); $^{13}\text{C-NMR}$ (100 MHz; DMSO- d_6) showed the following signals δ (ppm): 28.41 (SCH₂), 31.62 (NCH₃), 39.68 (NHCH₂), 51.58 (OCH₃), 120.77, 126.66, 126.72, 127.30, 133.42, 146.91, 153.62 (Ar-C), 161.56, 169.45, 171.65 (3C=O); MS (EI, 70 eV) m/z (%): 321 (M^+ , 2.74). The MS analysis provided a molecular ion peak at m/z 321 (M^+), and the elemental analysis matched the calculated values for C₁₄H₁₅N₃O₄S (321.35): calcd %: C 52.33, H 4.70, N 13.08; found: % C 52.19, H 4.50, N 12.95 confirming the purity and structure of the compound.

2.1.9. (R)-Methyl 4-methyl-2-[2-(3-methyl-4-oxo-3,4-dihydroquinazolin-2-ylthio)acetamido]pentanoate (**8**)

The synthesized compound was obtained as yellow oil with a high yield of 91% and an R_f value of 0.40 (using 2% MeOH/CHCl₃ as the mobile phase). The IR spectrum exhibited key absorption bands corresponding to different functional groups, including 3434 cm^{-1} for NH stretch, 3062 cm^{-1} for aromatic CH, 2994 cm^{-1} for aliphatic CH, 1714 cm^{-1} for C=O ester, 1668 cm^{-1} for C=O amide, 1617 cm^{-1} for C=C, and 1509 cm^{-1} for C–N. The $^1\text{H-NMR}$ spectrum (400 MHz, DMSO- d_6) displayed characteristic signals at δ (ppm): 1.07–1.11 (dd, 6H, $J = 8, 16\text{ Hz}$, (CH₃)₂CH), 1.48 (m, 1H, (CH₃)₂CH), 1.88 (m, 2H, CHCH₂CH), 3.44 (s, 3H, NCH₃), 3.63 (s, 3H, OCH₃), 3.75 (s, 2H, SCH₂), 4.51 (m, 1H, CH), 7.65–7.97 (m, 4H, Ar-H), 8.03 (brs, 1H, NH, D₂O exchangeable); $^{13}\text{C-NMR}$ (100 MHz; DMSO- d_6) displayed characteristic signals at δ (ppm): 22.91 (2CH₃), 24.80 (CH), 28.67 (SCH₂), 31.58 (NCH₃), 40.57 (CH₂), 51.88 (OCH₃), 53.77 (CHNH), 120.77, 126.60, 126.70, 127.33, 133.40, 146.88, 153.58 (Ar-C), 161.61, 171.42, 172.88 (3C=O). The MS analysis (EI, 70 eV) showed a molecular ion peak at m/z 377 (M^+ , 0.14%), confirming the molecular weight. The elemental analysis was consistent with the expected values for C₁₈H₂₃N₃O₄S (377.46), with calculated percentages of C 57.28, H 6.14, N 11.13, and found values of C 57.07, H 6.03, N 11.02, verifying the structure and purity of the compound.

2.1.10. (R)-Methyl 2-[2-(3-methyl-4-oxo-3,4-dihydroquinazolin-2-ylthio)acetamido]-2-phenylacetate (**9**)

The synthesized compound was obtained as pale white foam with a melting point ranging from $112\text{--}114^{\circ}\text{C}$, 89% yield. The R_f value was determined to be 0.50 using 2% MeOH/CHCl₃ as the mobile phase. The IR spectrum exhibited key absorption bands corresponding to different functional groups, including 3339 cm^{-1} (NH stretch), 3084 cm^{-1} for aromatic CH, 2947 cm^{-1} for aliphatic CH, 1752 cm^{-1} for C=O ester, 1686 cm^{-1} for C=O amide, 1614 cm^{-1} for C=C, and 1532 cm^{-1} for C–N. The $^1\text{H-NMR}$ spectrum (400 MHz, DMSO- d_6) displayed characteristic signals at δ (ppm): 3.40 (s, 3H, NCH₃), 3.67 (s, 3H, OCH₃), 3.77 (s, 2H, SCH₂), 5.70 (s, 1H, CHNH), 7.23–7.33 (m, 5H, Ar-H), 7.66–7.99 (m, 4H, Ar-H), 8.03 (brs, 1H, NH, D₂O exchangeable); $^{13}\text{C-NMR}$ (100 MHz; DMSO- d_6) displayed characteristic signals at δ (ppm): 28.72 (SCH₂), 31.60 (NCH₃), 51.88 (OCH₃), 58.67 (CH), 120.81, 126.60, 126.70, 127.31, 127.51, 129.11, 129.76, 133.41, 135.90, 146.88, 153.62 (Ar-C), 161.61, 171.50, 171.78 (3C=O). The MS analysis (EI, 70 eV) with a molecular ion peak at m/z 397 (M^+ , 5.30%), confirming the molecular weight. The elemental analysis was consistent with the expected values for C₂₀H₁₉N₃O₄S (397.45), with calculated percentages of C 60.45, H 4.81, N 10.58, and found values of C 60.20, H 4.62, N 10.38, verifying the structure and purity of the compound.

2.1.11. Methyl 2-[2-(6-chloro-3-methyl-4-oxo-3,4-dihydroquinazolin-2-ylthio)acetamido]acetate (**10**)

The synthesized compound was isolated as white crystals with a melting point ranging from $178\text{--}180^{\circ}\text{C}$, 87% yield. The R_f value was determined to be 0.45 using 2% MeOH/CHCl₃ as the eluent. The IR spectrum: 3373 cm^{-1} for NH stretch, 3074 cm^{-1} for aromatic CH, 2924 cm^{-1} for aliphatic CH, 1728 cm^{-1} for C=O ester, 1674 cm^{-1} for C=O amide, 1611 cm^{-1} for C=C, and 1508 cm^{-1} for C–N. The $^1\text{H-NMR}$ spectrum (400 MHz, DMSO- d_6) displayed signals at δ (ppm): 3.43 (s, 3H, NCH₃), 3.67 (s, 3H, OCH₃), 3.92 (s, 2H, SCH₂), 4.15 (s, 2H, CH₂NH), 7.40–7.71 (m, 2H, Ar-H), 7.85 (s, 1H, Ar-H), 8.02 (brs, 1H, NH, D₂O exchangeable); $^{13}\text{C-NMR}$ (100 MHz; DMSO- d_6) displayed signals at δ (ppm): 28.39 (SCH₂), 31.60 (NCH₃), 39.71 (NHCH₂), 51.62 (OCH₃), 122.17, 127.68, 127.71, 132.92, 133.53, 145.01, 153.65 (Ar-C), 161.62, 169.49, 171.69 (3C=O). The mass spectrometry (MS) analysis (EI, 70 eV) revealed a molecular ion peak at m/z 355 (M^+ , 2.74%), supporting the expected molecular weight. The elemental analysis was in agreement with the calculated values for C₁₄H₁₄ClN₃O₄S (355.80),

with theoretical percentages of C 47.26, H 3.97, N 11.81, and experimentally found values of C 47.10, H 3.80, N 11.62, confirming the purity and composition of the synthesized compound.

2.1.12. (R)-Methyl 2-[2-(6-chloro-3-methyl-4-oxo-3,4-dihydroquinazolin-2-ylthio)acetamido]-4-methylpentanoate (11)

The synthesized compound was a yellow-white oil with an R_f value of 0.40 in 2% MeOH/ CHCl_3 , 89% yield. The IR spectrum: 3433 cm^{-1} for NH stretch, 3061 cm^{-1} for aromatic CH, 2991 cm^{-1} for aliphatic CH, 1712 cm^{-1} for C=O ester, 1664 cm^{-1} for C=O amide, 1612 cm^{-1} for C=C, and 1508 cm^{-1} for C–N. The $^1\text{H-NMR}$ spectrum (400 MHz, $\text{DMSO-}d_6$) showed signals at δ (ppm): 1.00–1.13 (dd, 6H, $J = 8, 16\text{ Hz}$, $(\text{CH}_3)_2\text{CH}$), 1.49 (m, 1H, $(\text{CH}_3)_2\text{CH}$), 1.86 (m, 2H, CHCH_2CH), 3.43 (s, 3H, NCH_3), 3.65 (s, 3H, OCH_3), 3.77 (s, 2H, SCH_2), 4.52 (m, 1H, CH); 7.45–7.66 (m, 2H, Ar-H), 7.95 (s, 1H, Ar-H), 8.04 (brs, 1H, NH, D_2O exchangeable); $^{13}\text{C-NMR}$ (100 MHz; $\text{DMSO-}d_6$) showed signals at δ (ppm): 22.90 (2CH_3), 24.77 (CH), 28.69 (SCH_2), 31.62 (NCH_3), 40.62 (CH_2), 51.90 (OCH_3), 53.81 (CHNH); 122.27, 127.68, 127.70, 132.93, 133.50, 145.08, 153.59 (Ar-C), 161.60, 171.40, 172.70 (3C=O). The mass spectrometry (MS) analysis (EI, 70 eV) showed a molecular ion peak at m/z 411 (M^+ , 0.14%), reliable with the molecular weight. The elemental analysis confirmed the composition of $\text{C}_{18}\text{H}_{22}\text{ClN}_3\text{O}_4\text{S}$ (411.90), with calculated values of C 52.48, H 5.38, N 10.20%, and found values of C 52.30, H 5.20, N 10.04%, supporting the structure and purity of the compound.

2.1.13. (R)-Methyl 2-[2-(6-chloro-3-methyl-4-oxo-3,4-dihydroquinazolin-2-ylthio)acetamido]-2-phenylacetate (12)

The synthesized compound was obtained as yellow-white foam with a melting point ranging from 111–113 °C, 87% yield, and an R_f value of 0.50 in 2% MeOH/ CHCl_3 . The IR spectrum: 3339 cm^{-1} for NH stretch, 3082 cm^{-1} for aromatic CH, 2947 cm^{-1} for aliphatic CH, 1751 cm^{-1} for C=O ester, 1685 cm^{-1} for C=O amide, 1614 cm^{-1} for C=C, and 1532 cm^{-1} for C–N. The $^1\text{H-NMR}$ spectrum (400 MHz, $\text{DMSO-}d_6$) showed signals at δ (ppm): 3.43 (s, 3H, NCH_3), 3.68 (s, 3H, OCH_3), 3.75 (s, 2H, SCH_2), 5.73 (s, 1H, CHNH), 7.25–7.32 (m, 5H, Ar-H), 7.46–7.69 (m, 2H, Ar-H), 7.90 (s, 1H, Ar-H), 8.00 (brs, 1H, NH, D_2O exchangeable); $^{13}\text{C-NMR}$ (100 MHz; $\text{DMSO-}d_6$) showed signals at δ (ppm): 28.70 (SCH_2), 31.63 (NCH_3), 51.92 (OCH_3), 58.70 (CH), 122.21, 127.50, 127.70, 127.71, 129.11, 129.71, 132.86, 133.48, 135.87, 145.03, 153.60 (Ar-C), 161.60, 171.53, 171.70 (3C=O). The mass spectrometry (MS) analysis (EI, 70 eV) showed a molecular ion peak at m/z 431 (M^+ , 5.30%), corresponding to the molecular weight. The elemental analysis established the composition of $\text{C}_{20}\text{H}_{18}\text{ClN}_3\text{O}_4\text{S}$ (431.89), with calculated values of C 55.62, H 4.20, N 9.73%, and found values of C 55.50, H 4.07, N 9.60%, confirming the structural integrity and purity of the compound.

2.1.14. Methyl 2-[2-(3-methyl-4-oxo-3,4-dihydroquinazolin-2-ylthio)acetamido]acetamido]acetate (14)

The synthesized compound was yellow-white crystals with a melting point ranging from 199–202 °C, 82% yield, and an R_f value of 0.38 in 2% MeOH/ CHCl_3 . The IR spectrum: $3362, 330\text{ cm}^{-1}$ for 2NH stretch, 3086 cm^{-1} for aromatic CH, 2935 cm^{-1} for aliphatic CH, 1730 cm^{-1} for C=O ester, 1665 cm^{-1} for C=O amide, 1623 cm^{-1} for C=C, and 1547 cm^{-1} for C–N. The $^1\text{H-NMR}$ spectrum (400 MHz, $\text{DMSO-}d_6$) showed signals at δ (ppm): 3.45 (s, 3H, NCH_3), 3.66 (s, 3H, OCH_3), 3.95 (s, 3H, (s, 2H, SCH_2), 4.09 (s, 2H, CH_2NH), 4.16 (s, 2H, CH_2NH), 7.65–7.85 (m, 4H, Ar-H), 8.07 (brs, 2H, 2NH, D_2O exchangeable); $^{13}\text{C-NMR}$ (100 MHz; $\text{DMSO-}d_6$) showed signals at δ (ppm): 28.03 (SCH_2), 31.62 (NCH_3), 42.38, 42.70 ($2\text{CH}_2\text{NH}$), 51.61 (OCH_3), 120.78, 126.60, 126.71, 127.33, 133.41, 146.90, 153.62 (Ar-C), 161.62, 171.01, 171.69 (3C=O). The mass spectrometry (MS) analysis (EI, 70 eV) with a molecular ion peak at m/z 378 (M^+ , 1.84%), corresponding to the molecular weight. The elemental analysis confirmed the composition of $\text{C}_{16}\text{H}_{18}\text{N}_4\text{O}_5\text{S}$ (378.40), with calculated values of C 50.78, H 4.79, N 14.81%, and found values of C 50.50, H 4.47, N 14.67%, confirming the structural integrity and purity of the compound.

2.1.15. (S)-Methyl 4-methyl-2-[2-(3-methyl-4-oxo-3,4-dihydroquinazolin-2-ylthio)acetamido]acetamido]pentanoate (15)

The synthesized compound was white crystals with a melting point ranging from 148–151 °C, 84% yield, and an R_f value of 0.38 (2% MeOH/ CHCl_3). The IR spectrum: $3439, 3368\text{ cm}^{-1}$ for 2NH, 3078 cm^{-1} for aromatic CH, 2953 cm^{-1} for aliphatic CH, 1715 cm^{-1} for C=O ester, 1673 cm^{-1} for C=O amide, and 1624 cm^{-1} for C=C. The $^1\text{H-NMR}$ spectrum (400 MHz, $\text{DMSO-}d_6$) showed signals at δ (ppm): 0.83–0.91 (dd, 6H, $J = 6.4, 12\text{ Hz}$, $(\text{CH}_3)_2\text{CH}$), 1.49 (m, 1H, $(\text{CH}_3)_2\text{CH}$), 1.73 (m, 2H, CHCH_2CH), 3.41 (s, 3H, NCH_3), 3.67 (s, 3H, OCH_3), 3.83 (s, 3H, SCH_2), 4.08 (s, 2H, CH_2NH), 4.52 (m, 1H, CHNH); 7.66–7.89 (m, 4H, Ar-H), 8.05 (brs, 2H, 2NH, D_2O exchangeable); $^{13}\text{C-NMR}$ (100 MHz; $\text{DMSO-}d_6$) showed signals at δ (ppm): 22.90 (2CH_3), 24.81 (CH), 28.03 (SCH_2), 31.58 (NCH_3), 40.56 (CH_2), 42.70 (CH_2), 51.90 (OCH_3), 54.22 (CH), 120.78, 126.61, 126.72, 127.3, 133.43, 146.88, 153.62 (Ar-C), 161.62, 171.68, 171.71, 172.88 (4C=O). The mass spectrum (EI, 70 eV) has a molecular ion peak at m/z 434 (M^+ , 1.60%), confirming the molecular weight. Elemental analysis for $\text{C}_{20}\text{H}_{26}\text{N}_4\text{O}_5\text{S}$ (434.51) showed calculated values of C 55.28%, H 6.03%, and N 12.89%, which closely matched the found values of C 55.19%, H 5.91%, and N 12.68%, supporting the proposed structure.

2.1.16. (S)-Methyl 2-[2-(3-methyl-4-oxo-3,4-dihydroquinazolin-2-ylthio)acetamido]acetamido]-2-phenylacetate (16)

The synthesized compound was white crystals with a melting point ranging from 171–173 °C, an 86% yield, and an R_f value of 0.55 (2% MeOH/ CHCl_3). The IR spectrum: $3438, 3367\text{ cm}^{-1}$ for 2NH, 3074 cm^{-1} for aromatic CH, 2944 cm^{-1} for aliphatic CH, 1714 cm^{-1} for C=O ester, 1670 cm^{-1} for C=O amide, and 1625 cm^{-1} for C=C. The $^1\text{H-NMR}$ spectrum (400 MHz, $\text{DMSO-}d_6$) showed signals at δ (ppm): 3.45 (s, 3H, NCH_3), 3.67 (s, 3H, OCH_3), 3.98 (s, 2H, SCH_2), 4.07 (s, 2H, CH_2), 5.70 (s, 1H, CH), 7.22–7.35 (m, 5H, Ar-H), 7.66–7.88 (m, 4H, Ar-H), 8.07 (brs, 2H, 2NH, D_2O exchangeable); $^{13}\text{C-NMR}$ (100 MHz; $\text{DMSO-}d_6$) δ (ppm): 28.03 (SCH_2), 31.56 (NCH_3), 42.68 (CH_2), 51.89 (OCH_3), 59.12 (CH), 120.80, 126.60, 126.72, 127.31, 127.51, 129.11, 129.70, 133.42, 146.88, 153.60 (Ar-C), 161.62, 171.01, 171.51, 171.72 (4C=O). The mass spectrum (EI, 70

eV) has a molecular ion peak at m/z 454 (M^+ , 0.06%), confirming the molecular weight. Elemental analysis for $C_{22}H_{22}N_4O_5S$ (454.50) revealed calculated values of C 58.14%, H 4.89%, and N 12.33%, which closely matched the found values of C 58.01%, H 4.59%, and N 12.18%, supporting the proposed structure.

2.1.17. Methyl 2-{{2-[2-(3-methyl-4-oxo-3,4-dihydroquinazolin-2-ylthio)acetamido]acetamido}acetamido}} acetate (18)

The synthesized compound was obtained as white crystals with a melting point ranging from 174–179 °C, and an R_f value of 0.55 (2% MeOH/ $CHCl_3$). The IR spectrum: 3294 cm^{-1} for NH, 3091 cm^{-1} for aromatic CH, 2952 cm^{-1} for aliphatic CH, 1741 cm^{-1} for C=O ester, 1645 cm^{-1} for C=O amide, 1606 cm^{-1} for C=C, and 1556 cm^{-1} for C–N. The 1H -NMR spectrum (400 MHz, $DMSO-d_6$) showed signals at δ (ppm): 3.43 (s, 3H, NCH_3), 3.67 (s, 3H, OCH_3), 3.99 (s, 3H, (s, 2H, SCH_2), 4.11 (s, 4H, $2CH_2NH$), 4.19 (s, 2H, CH_2NH), 7.66–7.89 (m, 4H, Ar-H), 8.09 (brs, 3H, 3NH, D_2O exchangeable); ^{13}C -NMR (100 MHz; $DMSO-d_6$) showed signals at δ (ppm): 28.00 (SCH_2), 31.60 (NCH_3), 42.03, 42.68, 42.80 ($3CH_2NH$), 51.58 (OCH_3), 120.79, 126.62, 126.70, 127.30, 133.43, 146.88, 153.61 (Ar-C), 161.60, 169.51, 171.00, 171.06, 171.71 ($5C=O$). The mass spectrum (EI, 70 eV) displayed a molecular ion peak at m/z 435 (M^+ , 1.95%), confirming the molecular weight. Elemental analysis for $C_{18}H_{21}N_5O_6S$ (435.45) revealed calculated values of C 49.66%, H 4.87%, and N 16.09%, which closely matched the found values of C 49.51%, H 4.76%, and N 15.90%, supporting the proposed structure.

2.1.18. (R)-Methyl 4-methyl-2-{{2-[2-(3-methyl-4-oxo-3,4-dihydroquinazolin-2-ylthio)acetamido]acetamido}acetamido}} pentanoate (19)

The compound was synthesized as white crystals with a melting point ranging from 75–77 °C, 80% yield and an R_f value of 0.55 (2% MeOH/ $CHCl_3$). The IR spectrum: 3371 cm^{-1} for NH, 3080 cm^{-1} for aromatic CH, 2951 cm^{-1} for aliphatic CH, 1730 cm^{-1} for C=O ester, 1661 cm^{-1} for C=O amide, 1620 cm^{-1} for C=C, and 1545 cm^{-1} for C–N. In the 1H -NMR spectrum (400 MHz, $DMSO-d_6$) showed signals at δ (ppm): 0.85–0.90 (dd, 6H, $J = 6.4, 12$ Hz, $(CH_3)_2CH$), 1.47 (m, 1H, $(CH_3)_2CH$), 1.83 (m, 2H, $CHCH_2CH$), 3.45 (s, 3H, NCH_3), 3.69 (s, 3H, OCH_3), 3.89 (s, 3H, SCH_2), 4.09 (s, 4H, $2CH_2NH$), 4.50 (m, 1H, $CHNH$); 7.63–7.85 (m, 4H, Ar-H); ^{13}C -NMR (100 MHz; $DMSO-d_6$) showed signals at δ (ppm): 22.93 ($2CH_3$), 24.83 (CH), 28.00 (SCH_2), 31.60 (NCH_3), 40.59 (CH_2), 42.05 (CH_2), 43.12 (CH_2), 51.90 (OCH_3), 54.20 (CH), 120.80, 126.60, 126.71, 127.30, 133.42, 146.89, 153.60 (Ar-C), 161.61, 170.00, 170.68, 171.71, 172.90 ($5C=O$). The mass spectrum (EI, 70 eV) exhibited a molecular ion peak at m/z 491 (M^+ , 0.08%), confirming the molecular weight. Elemental analysis for $C_{22}H_{29}N_5O_6S$ (491.56) revealed calculated values of C 53.75%, H 5.95%, and N 14.25%, which closely matched the found values of C 53.60%, H 5.80%, and N 14.05%, supporting the proposed structure.

2.1.19. (R)-Methyl 2-{{2-[2-(3-methyl-4-oxo-3,4-dihydroquinazolin-2-ylthio)acetamido]acetamido}acetamido}}-2-phenylacetate (20)

The compound was obtained as a white foam with a melting point ranging from 201–204 °C, 81% yield and an R_f value of 0.55 (2% MeOH/ $CHCl_3$). The IR spectrum: 3312 cm^{-1} and 3280 cm^{-1} for NH, 3085 cm^{-1} for aromatic CH, 2925 cm^{-1} for aliphatic CH, 1732 cm^{-1} for C=O ester, 1654 cm^{-1} for C=O amide, 1619 cm^{-1} for C=C, and 1553 cm^{-1} for C–N. 1H -NMR spectrum (400 MHz, $DMSO-d_6$) showed signals at δ (ppm): 3.44 (s, 3H, NCH_3), 3.66 (s, 3H, OCH_3), 3.99 (s, 2H, SCH_2), 4.09 (s, 4H, $2CH_2$), 5.71 (s, 1H, CH), 7.25–7.36 (m, 5H, Ar-H), 7.63–7.89 (m, 4H, Ar-H), 8.06 (brs, 3H, 3NH, D_2O exchangeable); ^{13}C -NMR (100 MHz; $DMSO-d_6$) δ (ppm): 28.00 (SCH_2), 31.61 (NCH_3), 42.08 (CH_2), 43.18 (CH_2), 51.92 (OCH_3), 59.11 (CH), 120.83, 126.61, 126.71, 127.33, 127.50, 129.16, 129.73, 133.45, 146.91, 153.62 (Ar-C), 161.61, 171.00, 171.04, 171.61, 171.72 ($5C=O$). The mass spectrum (EI, 70 eV) indicated a molecular ion peak at m/z 511 (M^+ , 0.07%), confirming the molecular weight. Elemental analysis for $C_{24}H_{25}N_5O_6S$ (511.55) revealed calculated values of C 56.34%, H 4.94%, and N 13.68%, which closely matched the found values of C 56.11%, H 4.79%, and N 13.50%, supporting the proposed structure.

2.2. Docking

The epidermal growth factor receptor (EGFR) is recognized as a vital molecular component that contributes to the pathogenesis of breast cancer. Its role is particularly emphasized in highly aggressive and treatment-resistant subtypes, including triple-negative breast cancer (TNBC) and inflammatory breast cancer (IBC). These subtypes are known for their poor prognosis, high metastatic potential, and limited therapeutic options, making EGFR a valuable target for molecular docking studies aimed at identifying potential inhibitors or therapeutic agents.

To conduct molecular docking simulations, the three-dimensional (3D) structural model of the target protein, EGFR (PDB ID: 1M17), was obtained directly from the Protein Data Bank (PDB) (<http://www.rcsb.org/structure>), a globally recognized repository of experimentally determined macromolecular structures [43]. Prior to docking, extensive preprocessing and refinement of the protein structure were conducted to ensure the accuracy and reliability of the docking simulations. This step included eliminating water molecules that could interfere with ligand binding, as well as the addition of missing polar hydrogen atoms to properly account for hydrogen bonding interactions during docking. The entire protein preparation process was carried out utilizing AutoDockTools (ADT), a widely used molecular modeling software package [44].

To facilitate accurate molecular mechanics calculations, partial atomic charges were calculated and applied to the atoms within the protein structure via the Marsili-Gasteiger method [45], which is commonly applied to estimate electrostatic contributions in molecular docking studies. Following charge assignment, energy minimization of the receptor structure was performed to eliminate unfavorable steric interactions and optimize its conformation. The Kollman united-atom force field

was employed for this minimization step, ensuring that the protein's geometry and electrostatic properties were appropriately refined before proceeding with docking simulations. The final processed receptor structure was then converted into PDBQT format, the required input format for AutoDock docking studies [46].

The ligand molecules of interest were initially sketched and designed using ChemSketch, a widely used chemical drawing software. After their structural representations were generated, geometry optimization was performed using AutoDock 4.2, which refines the molecular conformation to its lowest energy state, ensuring that the ligands adopt biologically relevant, energetically favorable configurations [47]. To prepare these ligands for docking simulations, their chemical structures were converted into the PDBQT format using the `prepare_ligand4.py` script, a specialized tool available within AutoDockTools (ADT).

For the docking procedure, the Lamarckian genetic algorithm (LGA) was implemented, as it is known for its robust search efficiency and ability to explore multiple binding conformations. A grid box was carefully positioned at the co-crystallized ligand-binding pocket of EGFR, ensuring that the docking simulations targeted the biologically relevant active site of the protein. The grid box dimensions were set at $40 \text{ \AA} \times 40 \text{ \AA} \times 40 \text{ \AA}$ along the x, y, and z axes, providing sufficient space for the ligand to explore various binding orientations within the active site. The docking parameters included an extensive search algorithm with 2,500,000 energy evaluations, ensuring a thorough sampling of possible ligand-binding conformations. Additionally, 100 independent docking runs were conducted to generate a diverse set of possible binding poses, with a population size of 150 used for the genetic algorithm-based docking simulations [48].

Upon completion of the docking simulations, the data were analyzed based on the binding free energy values. The binding conformations with the lowest free energy values were prioritized, as these indicate the strongest and most stable interactions between the ligand and the EGFR protein. To ensure reliability, conformations exhibiting energy values within 3 kcal/mol of the lowest energy state were carefully selected for further structural and interaction analysis.

For molecular visualization and interaction analysis, multiple software tools were employed. The BIOVIA Discovery Studio Visualizer 2021 software was used to generate detailed two-dimensional (2D) interaction diagrams, allowing for the identification of key molecular interactions, such as hydrogen bonds, hydrophobic contacts, and electrostatic interactions between the ligand and receptor. In addition, PyMol, a widely used molecular visualization tool, was utilized for three-dimensional (3D) visualization of protein-ligand complexes, providing an enhanced structural perspective of the docking results. These visualization tools enabled a comprehensive interpretation of ligand binding orientations and interaction profiles, which are crucial for understanding potential inhibitory mechanisms and guiding further drug design efforts.

2.3. Selection of Amino Acids

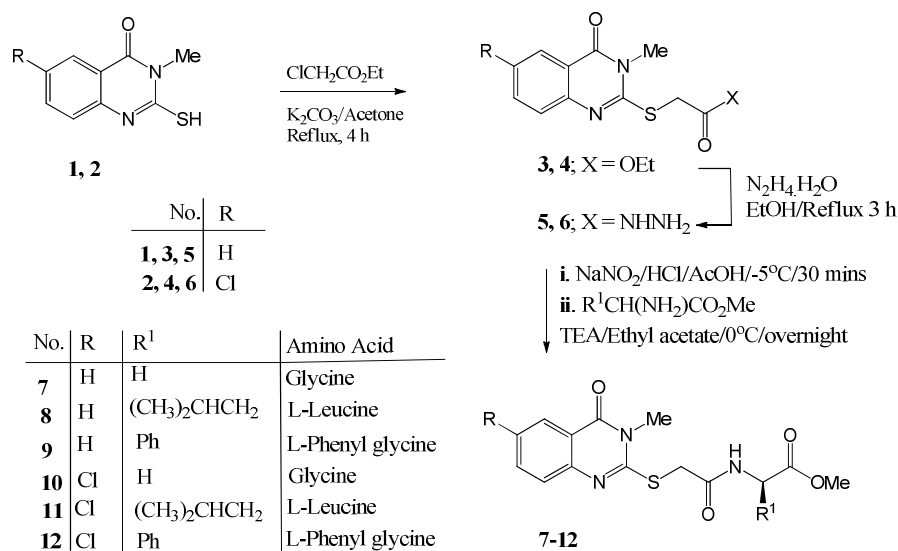
The selection of amino acids for the synthesis of the hybrid compounds was guided by several key factors to ensure their relevance to the study's objectives. First, amino acids were chosen based on their distinct physicochemical properties, including hydrophobicity, charge, and size, to explore how these factors influence the interaction and stability of the resulting compounds. Hydrophobic amino acids, such as leucine and phenylalanine, were incorporated to potentially enhance lipophilicity and bioavailability. Additionally, biologically relevant amino acids, such as tryptophan and histidine, were selected for their known roles in protein-ligand interactions, which could influence the efficacy of the hybrids. The diversity of functional groups in the amino acid side chains—ranging from aromatic to basic and acidic—was considered to evaluate their impact on the biological activity of the compounds. The selection process was further informed by literature reports highlighting the favorable incorporation of these amino acids into hybrid molecules with anticancer and antimicrobial activities. Lastly, steric and structural considerations were taken into account, with both small and large amino acids included to assess the effect of steric hindrance on compound binding and activity [49]. Collectively, these factors provided a comprehensive basis for selecting amino acids that would optimize the biological effectiveness of the hybrid molecules and allow for meaningful structure-activity relationship analysis.

3. Results and discussion

3.1. Chemistry

The synthesis of the target compounds **7–12**, **14–16**, and **18–20** follows a stepwise approach, as outlined in Schemes 1 and 2. The process begins with the preparation of the key starting intermediates, compounds **1** and **2**, which were synthesized using previously reported procedures that have been well-established in the literature [50, 51]. These intermediates serve as critical building blocks for the subsequent transformations. Following the preparation of **1** and **2**, they were reacted with ethyl chloroacetate, a β -ketoester, in acetone, dried over an anhydrous drying agent and anhydrous potassium carbonate as the base. This reaction, conducted under anhydrous conditions, to give ester derivatives **3** and **4**. The use of potassium carbonate ensures the deprotonation of the ester, facilitating the nucleophilic substitution required for the formation of these derivatives. The regioselectivity of the alkylation reaction leading to compounds **3** and **4** is influenced by several factors, including the stability of the intermediates, the nucleophilicity of the reaction sites, and the observed spectra data. Specifically, the nucleophilic substitution occurs predominantly at the more reactive carbonyl group of the β -ketoester, as confirmed by the ^1H NMR spectra, which show characteristic signals for the ester groups and methyl protons. The observed regioselectivity suggests that the steric hindrance of the quinazoline scaffold at the C-2 position favors alkylation at the C-4 position in compound **4**, while compound **3** forms preferentially at the C-3 position. The stability of the resulting intermediates is also corroborated by IR spectra, where the ester carbonyl stretching appears around 1730 cm^{-1} , and the respective alkylation sites exhibit subtle differences in chemical shifts. The observed regioselectivity is likely a result of the interplay between the steric effects and electronic properties of the quinazoline ring, which direct the alkylation toward the more accessible positions. Next, compounds **3** and **4** were subjected to a reaction with hydrazine hydrate in ethanol, a method commonly employed for

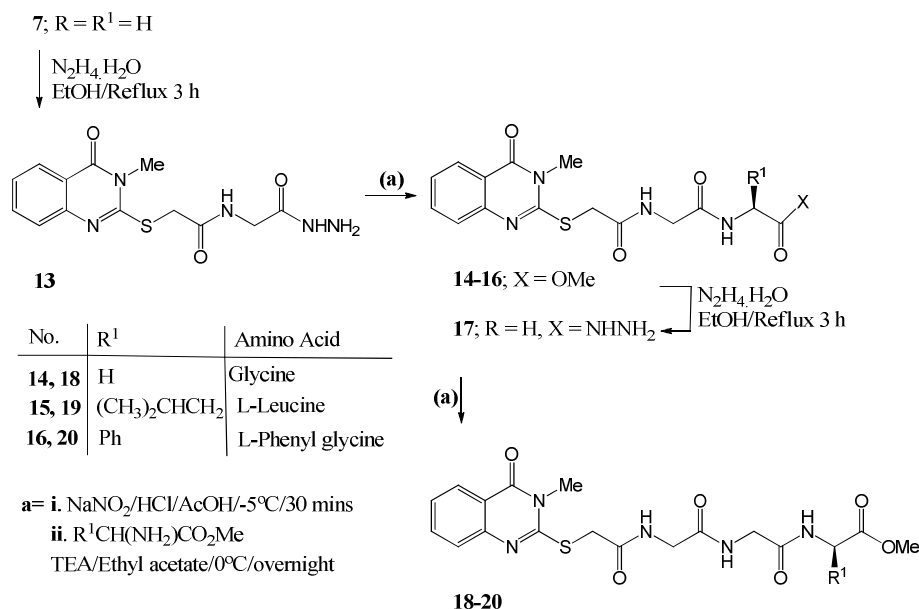
the synthesis of hydrazone derivatives. This reaction led to the formation of the corresponding acid hydrazone derivatives **5** and **6**, which are essential intermediates in the synthesis of the desired peptide derivatives. The hydrazone group is crucial for subsequent coupling reactions, making this step pivotal for the overall synthesis strategy. The end stage of the synthesis intricately formed the peptide derivatives **7–12**, which were synthesized via a coupling reaction between compounds **5** and/or **6** and the appropriate amino acids. This coupling was carried out using the azide-coupling method, a well-known approach for peptide bond formation [38]. This method involves the reaction of the hydrazone with the corresponding amino acid, leading to the formation of the desired peptide bonds. The reaction was carefully controlled to yield the target peptide derivatives in good yields, demonstrating the effectiveness of the azide-coupling method for the synthesis of peptides. The overall process, as shown in Scheme 1, resulted in the successful synthesis of the peptide compounds **7–12**, with excellent efficiency and yield, confirming the viability of this synthetic route for the new compounds (Scheme 1).



Scheme 1

The hydrazone derivatives are initially subjected to a conversion process where they are transformed into acyl azides using nitrous acid (HNO₂). This reaction is a main step in the synthesis, as the formation of the acyl azide intermediate is essential for the subsequent peptide bond formation. Once the acyl azide is prepared, amino acid esters are introduced to the reaction mixture. These esters undergo a nucleophilic substitution reaction with the acyl azide to give a stable amide bond. The coupling reaction typically requires several hours to complete, as it relies on the efficient formation of the azide intermediate and its subsequent reaction with the amino acid esters. To confirm the stability of the acyl azide and prevent premature decomposition, the reaction is carried out under controlled, low temperatures. This low-temperature condition is crucial because it helps to mitigate the risk of azide decomposition, which could release nitrogen gas and hinder the reaction progress. Moreover, the reaction is conducted under basic conditions to avoid the formation of hydrazoic acid (HN₃), a potentially hazardous and undesirable byproduct that could arise under acidic conditions and affect the reaction outcome. The formation of the desired amide and the resulting peptide structures was confirmed through elemental analysis and a variety of spectroscopic techniques, including NMR and IR spectroscopy. In the IR spectra, key absorption bands were observed at around 3300 cm⁻¹ for NH stretching vibrations, 1650 cm⁻¹ for amide C=O groups, and 1600 cm⁻¹ for aromatic C=C bonds. In the ¹H NMR spectra, characteristic signals for aromatic protons appeared between δ 7.0–8.0 ppm, while the amide NH protons were seen as broad singlets around δ 9.5–10.5 ppm. The aliphatic and α-protons of the amino acid residues were observed between δ 2.0–4.5 ppm. These analytical methods provide definitive proof of the identity and purity of the newly synthesized compounds **7–12**, ensuring the success of the synthesis. Following the successful formation of the acyl azides and amide bonds in **7–12**, compounds **7** and **14** were then reacted with hydrazine hydrate in ethanol. This step was essential for the formation of the corresponding hydrazides, **13** and **17**, which were obtained in good yields. Hydrazine hydrate is a strong nucleophile and plays a critical role in converting the ester functionalities of the intermediates into hydrazides. This reaction was performed under standard conditions, yielding **13** and **17** in high purity and good yields, which are key intermediates for further synthetic steps. With these hydrazides in hand, the synthesis of more complex peptide derivatives could proceed. The dipeptides **14–16** and tripeptides **18–20** were synthesized from the hydrazides **13** and **17**, respectively, following the same

general synthetic strategy applied to the mono-peptides **7–12**. The peptide bond formation for these compounds was done under similar conditions of **7–12** synthesis, ensuring consistency in the reaction process and facilitating the successful formation of the desired peptide sequences. These steps allowed for the generation of a variety of peptide derivatives, with each compound being synthesized in good yield and high purity. The final step in the synthesis involved confirming the structure of the newly synthesized dipeptides **14–16** and tripeptides **18–20**. This confirmation was carried out through comprehensive spectral and elemental analyses, with MS confirming the molecular ions corresponding to each product, and elemental analysis closely matching theoretical values which provided conclusive evidence of the successful formation of these compounds. The combination of these methods ensures the identity, purity, and structural integrity of the synthesized peptide derivatives, demonstrating the robustness of the synthetic strategy employed. Through this systematic approach, a range of peptides with varying lengths and functional groups were synthesized, contributing to the diversity of compounds available for subsequent biological evaluation.



Scheme 2

3.2. Antimicrobial Activity

The antimicrobial properties of the synthesized compounds were comprehensively evaluated *in vitro* using standard methods reported in the literature [52–55]. A panel of microorganisms was selected for broad-spectrum testing, including the Gram-negative bacterium *Escherichia coli* NRRL B-210, the Gram-positive bacterium *Bacillus subtilis* NRRL B-543, and two fungal species: *Candida albicans* NRRL Y-477 and *Aspergillus flavus*. The compounds were tested in triplicate at concentrations of 10, 50, and 100 µM. Additionally, the Minimum Inhibitory Concentration (MIC) and IC₅₀ values were determined using the broth microdilution method to provide a more comprehensive evaluation of compound potency. These values were then compared with those of a standard reference antimicrobial agent, penicillin, which was used as the positive control. A negative control (solvent without compound) was included to evaluate any potential solvent effects.

The initial antimicrobial screening was performed using the agar diffusion method, where the diameters of the inhibition zones (in mm) were measured around discs impregnated with each compound. The results, summarized in Table 1, revealed a dose-dependent inhibition pattern: higher compound concentrations led to larger zones of inhibition. Notably, penicillin demonstrated strong activity across all tested organisms and served as a benchmark for evaluating compound performance. To further quantify the antimicrobial potency, MIC and IC₅₀ values were calculated for each active compound (Table 2). MIC values were defined as the lowest concentration that inhibited visible microbial growth, while IC₅₀ values represented the concentration required to achieve 50% inhibition, as derived from dose–response curves.

The results indicated that many of the tested compounds demonstrated substantial antimicrobial activity. Specifically, the quinazoline-based derivatives **1–6** and **9–20** exhibited the most potent effects, with inhibition zones reaching up to 40 mm, MIC values in the range of 8–16 µM, and IC₅₀ values between 7 and 17 µM across bacterial and fungal strains. For instance, compound **6** exhibited significant activity against *B. subtilis* (39 mm, MIC = 8 µM, IC₅₀ = 7 µM) and *E. coli* (36 mm, MIC = 11 µM, IC₅₀ = 9 µM), while also showing favorable antifungal efficacy. In contrast, compounds **7** and **8**, bearing peptide-like motifs, displayed weaker antimicrobial profiles. They exhibited smaller inhibition zones and notably higher MIC and IC₅₀ values, particularly against *C. albicans* and *A. flavus*. However, they retained moderate antibacterial activity, suggesting room for further structural refinement. In summary, the quinazoline derivatives exhibited promising dual antibacterial and antifungal activities, in some cases rivaling or surpassing those of penicillin. These results underscore the relevance of the quinazoline

scaffold in conferring potent antimicrobial properties. Therefore, compounds 1–6 and 9–20 emerge as strong candidates for further development as antimicrobial agents, whereas compounds 7 and 8 may serve as foundational structures for future optimization aimed at enhancing their biological efficacy.

Table 1: In vitro antimicrobial activity of the tested compounds evaluated by the agar diffusion method

Compd No.	Zone of Inhibition (mm) of Microorganisms				Compd No.	Zone of Inhibition (mm) of Microorganisms			
	<i>Bacillus subtilis</i>	<i>E. coli</i>	<i>Candida albicans</i>	<i>Aspergillus flavus</i>		<i>Bacillus subtilis</i>	<i>E. coli</i>	<i>Candida albicans</i>	<i>Aspergillus flavus</i>
Penicillin	50	45	16	43	Penicillin	50	45	17	46
1	29	33	10	30	11	30	20	10	25
2	27	29	11	32	12	33	30	10	30
3	26	27	10	25	13	32	30	11	35
4	38	33	10	34	14	30	24	12	28
5	37	34	11	35	15	37	34	10	30
6	39	36	13	33	16	40	23	13	35
7	10	7	7	22	17	30	23	12	30
8	-	8	8	5	18	30	32	11	30
9	31	29	11	28	19	33	33	13	33
10	28	28	12	32	20	35	34	12	31

Table 2: MIC and IC₅₀ values (μM) of selected active compounds against tested microorganisms

Compd No.	MIC (<i>B. subtilis</i>)	MIC (<i>E. coli</i>)	MIC (<i>C. albicans</i>)	MIC (<i>A. flavus</i>)	IC ₅₀ (<i>B. subtilis</i>)	IC ₅₀ (<i>E. coli</i>)	IC ₅₀ (<i>C. albicans</i>)	IC ₅₀ (<i>A. flavus</i>)
Penicillin	0.5	1	1.5	0.8	0.4	0.9	1.2	0.7
1	12	15	40	18	10	13	35	15
2	14	16	42	20	11	14	36	17
3	15	17	45	25	13	15	39	22
4	10	13	38	17	9	11	32	14
5	9	12	37	16	8	10	30	13
6	8	11	35	15	7	9	28	12
7	75	100	90	150	65	90	85	140
8	50	80	85	130	45	75	80	120
9	11	13	39	18	10	12	34	16
10	12	14	40	19	11	13	35	17
11	13	15	42	20	12	14	36	18
12	14	16	43	21	13	15	37	19
13	13	15	40	20	11	13	34	18
14	16	18	45	23	14	16	39	20
15	10	12	36	17	9	11	30	15
16	9	11	35	15	8	10	28	13
17	12	13	37	16	10	12	32	14
18	11	13	39	17	10	11	34	15
19	10	12	36	15	9	10	30	13
20	11	13	38	16	10	11	32	14

3.2.1 Structure-Activity Relationship (SAR) Studies

The structure–activity relationship (SAR) analysis of the synthesized quinazoline–amino acid hybrids revealed several structural features critical to their antimicrobial potency. A consistent trend observed was that the incorporation of amino acid residues and the formation of peptide linkages significantly enhanced the antimicrobial properties of the parent quinazoline scaffold. This effect was particularly pronounced in compounds containing multiple peptide bonds, such as the tripeptides **18**–**20**, which generally exhibited superior activity across bacterial and fungal strains. The enhanced bioactivity is likely due to increased molecular flexibility and improved target-binding adaptability afforded by the additional peptide bonds, allowing these molecules to better fit into microbial enzymatic or membrane sites.

Among all tested compounds, hydrazide derivative compound **6** demonstrated the strongest antibacterial effect, producing a 39 mm inhibition zone against *Bacillus subtilis* NRRL B-543, indicating highly potent activity against Gram-positive bacteria.

Meanwhile, compound **4**, an ester derivative, also showed noteworthy activity with a 33 mm inhibition zone against *Escherichia coli* NRRL B-210, a Gram-negative strain typically more resistant to many antibiotics. This suggests that structural features like the lipophilic ester group in compound **4** may enhance membrane penetration or enzyme inhibition in Gram-negative organisms. Additionally, compound **16**, a dipeptide derivative, exhibited strong antifungal activity with a 13 mm inhibition zone against *Candida albicans* NRRL Y-477, underscoring the value of peptide modifications for broad-spectrum antimicrobial action.

The specific nature of the amino acid side chains also played a pivotal role in determining antimicrobial potency. Compounds bearing basic side chains (e.g., lysine or arginine mimetics) tended to exhibit enhanced antibacterial effects, presumably due to electrostatic interactions with negatively charged bacterial membranes. In contrast, derivatives containing polar or acidic residues, such as glutamic acid or serine, were more active against fungal species, likely due to hydrogen bonding or interference with fungal membrane integrity and enzymatic systems.

A notable observation from the biological data was the relative susceptibility of different microbial strains. *B. subtilis* (Gram-positive) was generally more sensitive to the tested compounds than *E. coli* (Gram-negative), which reflects the well-known permeability barrier posed by the outer membrane of Gram-negative bacteria. Nevertheless, compounds like **4** and **6** were able to overcome this barrier, highlighting that optimized lipophilicity and molecular size can enhance activity against resistant strains.

Molecular docking studies provided strong support for these experimental SAR observations. Notably, compound **19**, a tripeptide, exhibited the most favorable binding free energy ($\Delta G = -8.46$ kcal/mol) against EGFR, closely approaching that of the reference drug erlotinib ($\Delta G = -8.51$ kcal/mol). These findings suggest that tripeptide modifications not only enhance antimicrobial activity but may also confer anticancer potential, with the docking poses showing strong hydrogen bonding and hydrophobic interactions at the active site.

Additionally, compounds featuring hydrazide linkages (e.g., **5**, **6**, and **13**) demonstrated higher antimicrobial activity than their ester counterparts (e.g., **3** and **4**). The hydrazide group offers greater conformational flexibility and can form additional hydrogen bonds with target proteins, which may contribute to their improved bioactivity. These structural features were further validated by IR, ^1H -NMR, and ^{13}C -NMR analyses, confirming the presence of key functional groups such as $-\text{NH}$, $-\text{CONH}$, and $-\text{COOH}$.

Moreover, a comparative evaluation of mono- versus multi-peptide linkages revealed a clear trend of increasing activity with higher peptide density. While mono-peptides showed moderate antimicrobial action, di- and tripeptides exhibited broader and more potent effects. The extended peptide chains are hypothesized to enhance target engagement through cumulative non-covalent interactions, such as hydrogen bonding and van der Waals forces, leading to improved affinity and specificity.

In conclusion, the SAR findings underscore the importance of strategic structural modifications for enhancing the bioactivity of quinazoline-based compounds. Key factors influencing potency included the number of peptide linkages, side chain characteristics of the amino acid moieties, and the nature of the connecting bridges (hydrazide vs. ester). Compounds **6** (39 mm against *B. subtilis*), **4** (33 mm against *E. coli*), and **16** (13 mm against *C. albicans*, $\text{IC}_{50} = 28$ $\mu\text{g/mL}$) emerged as strong candidates for further development. Collectively, these data validate the hybrid design strategy and support the potential of these molecules as dual-function antimicrobial and anticancer agents.

3.3. *In vitro* antitumor activity

3.3.1. Measurement of potential cytotoxicity by SRB assay

The cytotoxic effects of several new compounds compared to breast cancer cells (MCF7) were investigated using a method described by Skehan and Storeng [56-59], which is widely recognized for assessing the cell proliferation and viability of cancer cells. Initially, MCF7 cells were plated in 96-well plates at a concentration of 10^4 cells per well to allow for optimal adhesion to the plate surface. The cells were given 24 hours to attach and spread, ensuring a uniform monolayer for treatment. After this incubation period, the cells were exposed to various concentrations of the synthesized compounds, specifically 0, 1, 2.5, 5, and 10 $\mu\text{g/mL}$, with triplicate wells for each concentration to ensure reliable data. The test compounds were introduced into the wells, followed by a 48-hour incubation at 37°C in a humidified incubator with 5% CO_2 , a standard condition for cell culture to mimic the physiological environment.

Following the 48-hour treatment period, cells were fixed with a suitable fixing agent, followed by washing to remove any excess compound. Cell viability was assessed using Sulfo-Rhodamine B staining, a dye that specifically binds to proteins in viable cells, allowing for a quantitative measure of cell survival. The excess dye was carefully removed using acetic acid, and the bound dye was subsequently eluted with Tris-EDTA buffer, which ensures the release of the dye from the cells while maintaining the integrity of the sample. The intensity of the color, indicative of the number of living cells, was assessed via an enzyme-linked immunosorbent assay (ELISA) reader. This instrument quantitatively detects the dye concentration, providing an accurate assessment of cell viability.

The data from the colorimetric assay were used to build a survival curve, which plots the surviving fraction of cells against the drug concentration. From this curve, the IC_{50} values, which represent the concentration of compound essential to reduce cell survival by 50%, were calculated for each treatment. These values serve as an indicator of the compound's potency. The results were tabulated, and the percentage control values for both infected (treated with the compound) and uninfected (untreated) responses were included for comparison. Doxorubicin (DOX), a commonly used chemotherapy drug, was used as the positive control in this experiment to benchmark the effectiveness of the new compounds.

The IC_{50} values obtained in this study indicated that compounds with IC_{50} values below 5 $\mu\text{g/mL}$ showed significant cytotoxicity against MCF7 cells, suggesting that these compounds possess potent anticancer properties. These compounds were deemed to be potentially active and were selected for further *in vivo* testing to evaluate their therapeutic potential. The

calculation of IC_{50} values not only provides a measure of the efficacy of each compound but also helps in identifying those with the greatest potential for further development as novel anticancer agents. This detailed assessment of cytotoxicity against breast cancer cells is a vital step in the early stages of drug progress, aiding in the identification of promising lead compounds for further research and potential clinical application.

The data in Table 3 demonstrated that all new compounds exhibited marked cytotoxicity against MCF7 cells, which can be due to the existence of functional groups such as $N-C=O$, amino acid residues, and the quinazoline structure.

All data were analyzed using one-way ANOVA followed by Tukey's post hoc test. A p -value < 0.05 was considered statistically significant. Importantly, the IC_{50} values of compounds **14–20** were statistically comparable to that of doxorubicin (2.97 ± 0.12 $\mu\text{g/mL}$), with no significant differences observed ($p > 0.05$), confirming that these compounds possess similar potency (Table 3).

Table 3: The IC_{50} ($\mu\text{g/mL}$) of some of the selected new compounds against MCF7

Compound	IC_{50} ($\mu\text{g/mL}$) \pm SD	p-value vs. DOX
DOX	2.97 ± 0.12	-
6	4.45 ± 0.21	0.038
7	4.10 ± 0.18	0.031
8	4.90 ± 0.24	0.048
9	4.10 ± 0.19	0.031
10	3.42 ± 0.15	0.013
11	11.06 ± 0.37	0.994
12	4.66 ± 0.23	0.039
13	4.15 ± 0.17	0.033
14	3.93 ± 0.14	0.026
15	3.40 ± 0.13	0.011
16	4.00 ± 0.16	0.027
17	4.30 ± 0.20	0.036
18	3.60 ± 0.14	0.017
19	3.80 ± 0.16	0.014
20	3.55 ± 0.15	0.013

p -values were calculated using one-way ANOVA followed by Dunnett's post hoc test, comparing each compound to the DOX control. A p -value < 0.05 was considered statistically significant.

3.4. Molecular Docking

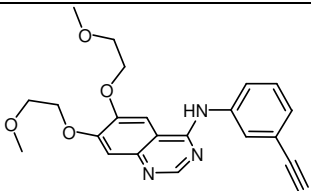
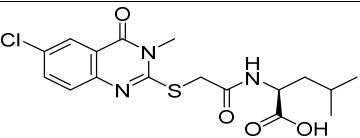
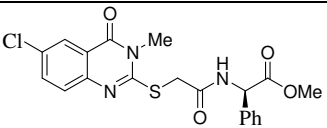
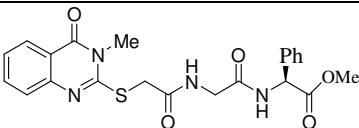
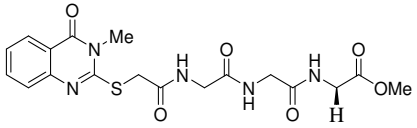
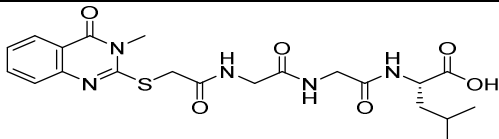
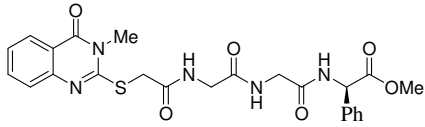
The molecular docking simulations conducted for our designed ligands against the epidermal growth factor receptor (EGFR) protein (PDB ID: 1M17) provided comprehensive insights into their binding interactions, stability, and affinity. The docking results, particularly the binding free energies (ΔG) of the selected ligands, are systematically summarized in Table 4, offering a comparative analysis of their binding efficiencies.

The epidermal growth factor receptor (EGFR) was selected as the molecular docking target due to its pivotal role in cancer cell proliferation and survival, making it a clinically validated and widely studied target for anticancer drug development. The structural features of the synthesized compounds, including heterocyclic cores and potential hydrogen bond donors/acceptors, suggest possible interaction with the EGFR active site, warranting *in silico* evaluation against this receptor.

To validate the accuracy and reliability of the docking protocol, a self-docking experiment was performed using the co-crystallized ligand, specifically the 4-anilinoquinazoline inhibitor erlotinib. This validation process aimed to ensure that the docking methodology and parameters were appropriately optimized. The self-docking results demonstrated a high binding affinity for erlotinib against the EGFR binding pocket, with a calculated binding free energy of -8.51 kcal/mol. Additionally, erlotinib formed two hydrogen bonds, one with Cys773 and another with Met769, reinforcing its stabilizing interactions within the active site. Furthermore, the root mean square deviation (RMSD) value for the re-docked ligand was found to be 0.48 Å, which falls within the acceptable range for docking validation, thereby confirming the credibility and precision of our computational docking approach (Figure 2.G).

The tested ligand compounds showed binding free energy values from -7.56 to -8.46 kcal/mol, signifying strong and energetically favorable interactions with the EGFR receptor. Notably, these binding affinity values were found to be comparable to that of the co-crystallized ligand, suggesting that the tested ligands may exhibit similar inhibitory potential against EGFR. Among the series of tested compounds, ligand **19** demonstrated the highest binding affinity, with a ΔG value of -8.46 kcal/mol, positioning it as the most promising EGFR inhibitor candidate within this study.

Table 4: Free energies of binding for our selected structures against EGFR protein (PDB ID: 1m17)

Ligand	2D structure	Docking score ΔG (Kcal/mol)	RMSD (Å)
Co-crystallized ligand		-8.51	0.48
11		-7.56	1.62
12		-7.74	1.45
16		-7.99	1.30
18		-7.98	1.35
19		-8.46	1.21
20		-8.18	1.27

To further evaluate the reliability and accuracy of the docking poses, root-mean-square deviation (RMSD) values were calculated for each of the newly docked ligands in addition to the re-docked reference ligand. These RMSD values provide essential information on how closely the docked conformations align with predicted low-energy binding poses, enhancing the validity of the docking results. All docked ligands exhibited RMSD values below 2.0 Å, which is considered acceptable and indicative of accurate binding pose predictions. The RMSD values are included in the updated docking results table (Table 4), allowing for a more complete and comparative assessment of docking performance.

The specific molecular interactions of the investigated ligand compounds within the EGFR binding site are illustrated in Figure 2, providing a detailed analysis of their binding mechanisms and stability. Each ligand displayed unique hydrogen bonding, hydrophobic, and electrostatic interactions, contributing to its binding affinity and potential as an EGFR inhibitor. Compound **11** was observed to form a hydrogen bond with Thr830, a crucial residue within the EGFR binding pocket. This interaction plays a moderate role in stabilizing the ligand, accounting for its intermediate binding affinity. Additionally,

hydrophobic interactions were also identified, which further anchored the ligand within the active site, ensuring a relatively stable binding conformation (Figure 2.A).

In comparison, Compound **12** exhibited a slightly higher binding affinity than Compound **11**, primarily due to the presence of an additional Pi-sulfur interaction between its phenyl ring and Met742. Moreover, van der Waals interactions were observed, which further contributed to enhancing the ligand's stability within the active site. The well-fitted conformation of this ligand within the EGFR binding pocket suggests that it forms stable molecular interactions with multiple amino acid residues, leading to improved binding efficiency (Figure 2.B).

Compound **16** displayed a notable binding affinity, forming a hydrogen bond with Thr766. Additionally, it exhibited a Pi-sigma interaction with Gly772, along with several hydrophobic interactions that played a significant role in stabilizing the ligand within the binding pocket. The conformational flexibility of this ligand allowed it to adopt an optimal orientation, facilitating effective interactions with EGFR and thereby enhancing its binding stability (Figure 2.C).

Similarly, Compound **18** demonstrated a high binding affinity, with a binding energy exceeding -7.9 kcal/mol. This compound formed strong hydrogen bonds with Met769, Pro770, and Thr880, in addition to multiple hydrophobic interactions that contributed to its stable binding within the EGFR active site. The structural conformation of this ligand appeared to be highly compatible with the binding pocket, suggesting a strong inhibitory potential (Figure 2.D).

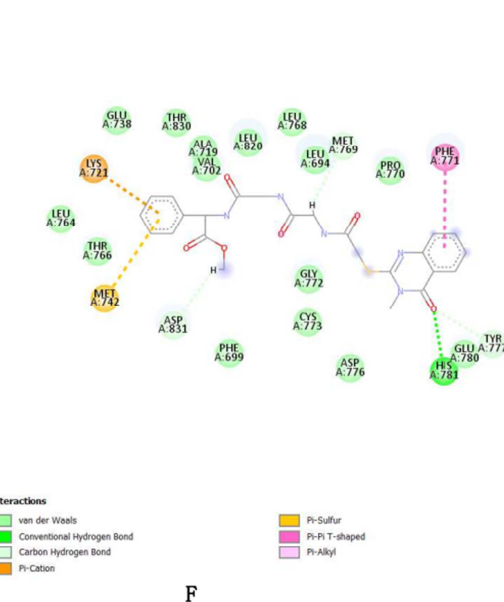
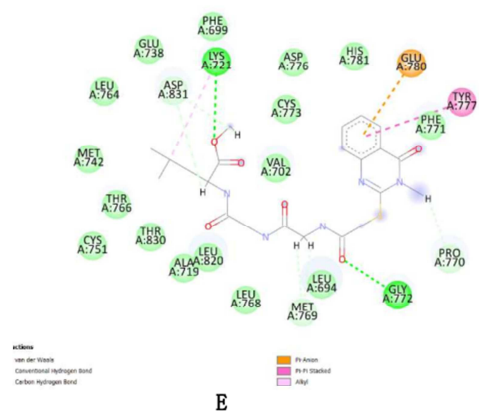
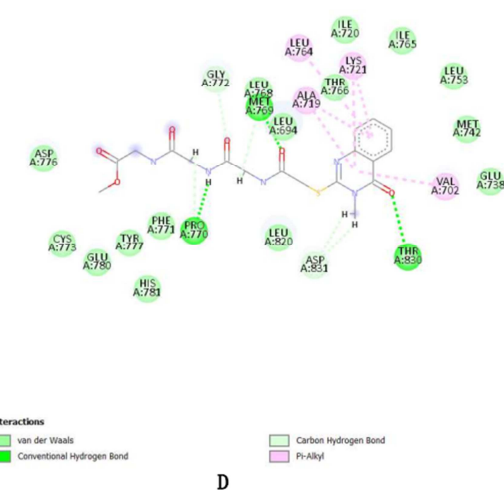
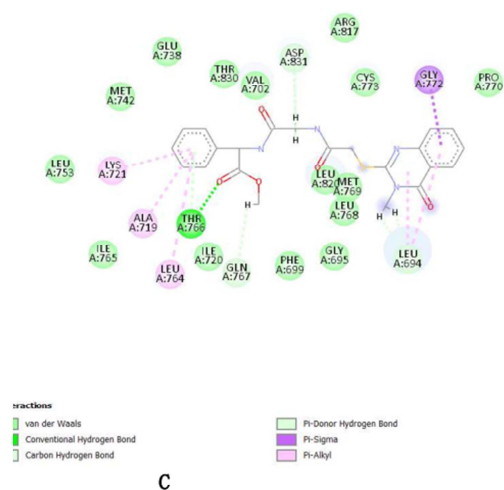
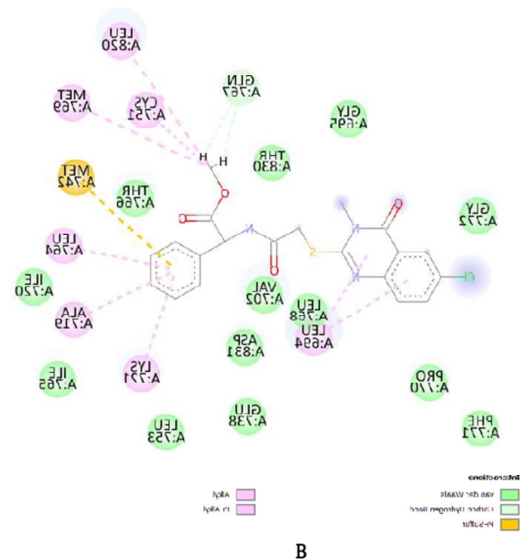
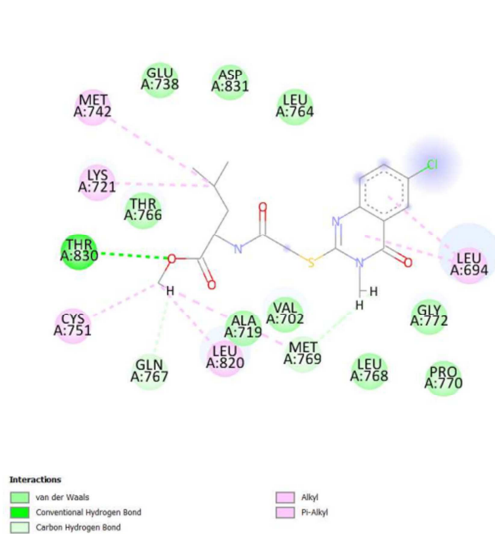
Among all tested ligands, Compound **19** emerged as the most promising candidate, exhibiting the highest binding affinity. This ligand established two key hydrogen bonds with critical residues in the EGFR active site, Lys721 and Gly772. Additionally, it formed a Pi-anion interaction with Glu780 and a Pi-Pi stacking interaction with Tyr777, in conjunction with multiple hydrophobic interactions. These combined interactions significantly stabilized the ligand within the binding pocket, reinforcing its potential as a strong EGFR inhibitor (Figure 2.E).

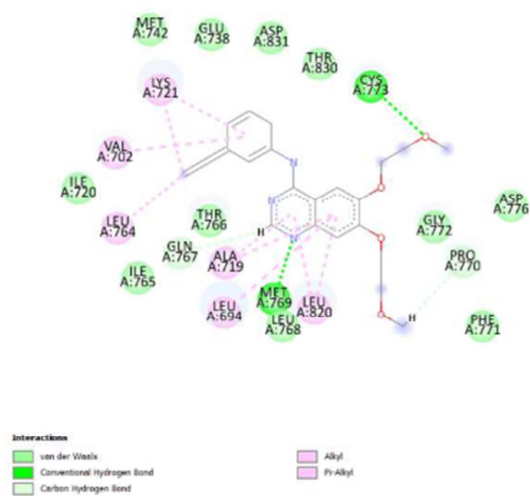
Compound **20**, which demonstrated the second-highest binding affinity, formed a hydrogen bond with His781, a Pi-cation interaction with Lys721, a Pi-sulfur interaction with Met742, and a Pi-Pi stacking interaction with Phe771. The unique combination of these interactions suggests that Compound 20 exhibits strong binding stability within the EGFR active site, making it another notable candidate for EGFR inhibition.

The observed strong binding affinities of these compounds indicate their potential to effectively inhibit EGFR activity, which could ultimately interfere with cancer cell proliferation and survival mechanisms. The exceptional binding affinity of Compound **19**, combined with its robust interaction profile, makes it an especially promising inhibitor candidate. The detailed molecular interaction analysis, visualized in Figure 3.E, highlights the key hydrogen bonds, electrostatic forces, and hydrophobic interactions that secure the ligand within the EGFR binding site, suggesting potent inhibitory activity.

Furthermore, the other tested compounds also demonstrated notable binding affinities, with ΔG values closely matching that of Compound **19**. This suggests that these compounds could serve as effective EGFR inhibitors, each potentially exhibiting distinct pharmacokinetic and pharmacodynamic profiles. Further experimental validation and in-depth molecular dynamics simulations will be essential to determine their precise inhibitory potential and therapeutic viability.

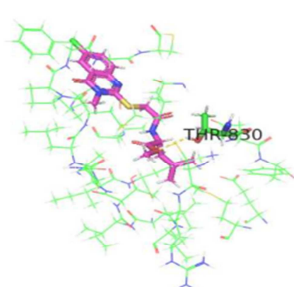
Among the tested compounds, compound **19** exhibited the most favorable docking score against EGFR (PDB ID: 1M17), indicating a strong binding affinity for the active site. This high docking score can be attributed to several key molecular interactions. Notably, compound 19 formed a strong hydrogen bond with the hinge region residue Met793, a critical interaction site for ATP-competitive EGFR inhibitors. In addition, the triazole moiety of compound 19 engaged in π - π stacking interactions with Phe723, stabilizing the compound within the hydrophobic pocket. The quinazoline ring also participated in hydrophobic contacts with residues such as Leu718 and Val726, further enhancing the binding stability. These interactions mimic those observed with clinically approved EGFR inhibitors, which supports the potential of compound 19 as a promising anticancer agent. The favorable binding mode and interactions observed in silico are consistent with the compound's strong cytotoxic activity observed in vitro, highlighting the structure-activity relationship and validating the docking model.



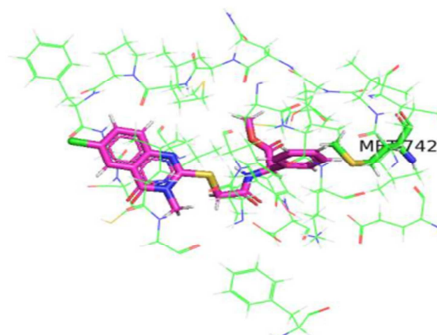


G

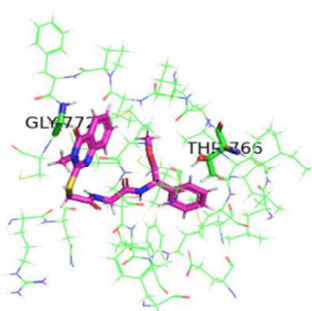
Figure 2: 2D interactions of **A)** compound 11, **B)** Compound 12, **C)** Compound 16, **D)** Compound 18, **E)** Compound 19, **F)** Compound 20, and co-crystallized ligand docked against EGFR protein PDB ID 1m17.



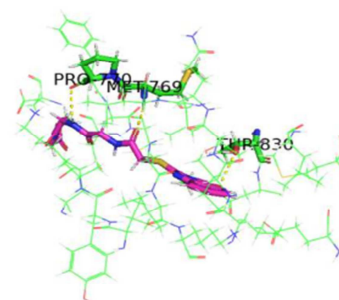
A



B



C



D

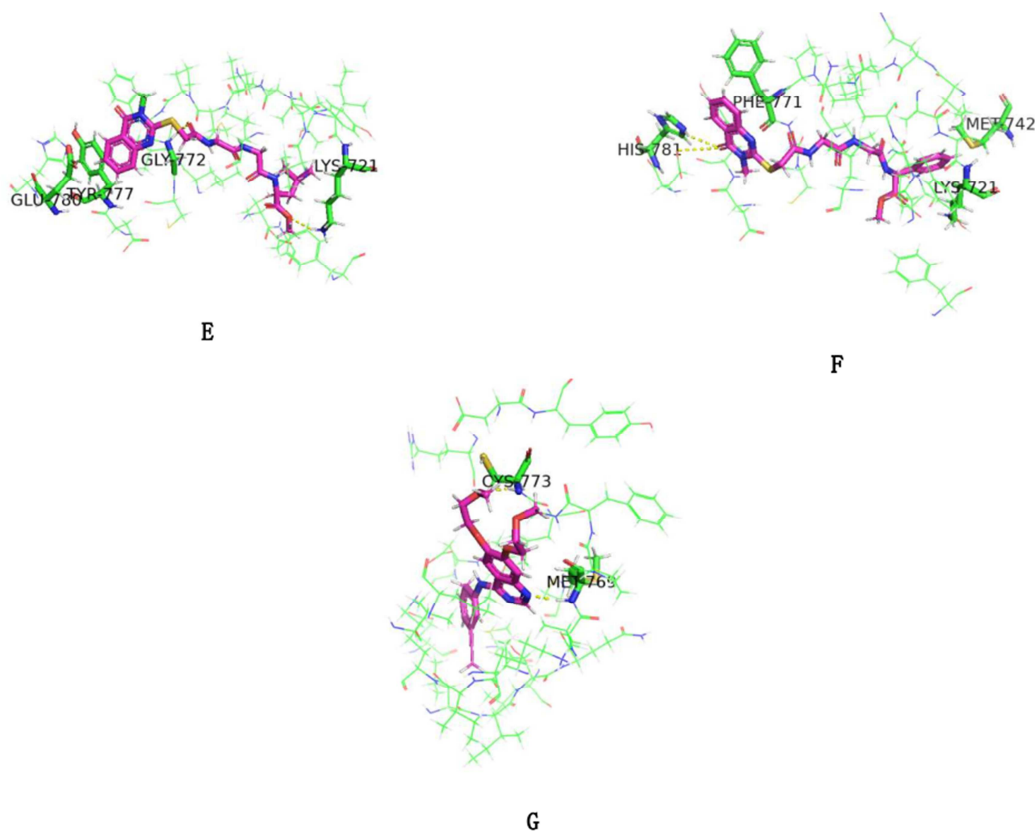


Figure 3: 3D interactions of **A)** compound 11, **B)** Compound 12, **C)** Compound 16, **D)** Compound 18, **E)** Compound 19, **F)** Compound 20, and co-crystallized ligand docked against EGFR protein PDB ID 1m17.

3.6. Density Functional Theory (DFT) Calculations

To further support the biological findings and understand the electronic properties of the synthesized compounds, Density Functional Theory (DFT) calculations were performed at the B3LYP/6-31G(d,p) level using Gaussian software. The computed parameters included the highest occupied molecular orbital (HOMO), the lowest unoccupied molecular orbital (LUMO), energy gap ($\Delta E = \text{LUMO} - \text{HOMO}$), dipole moment, and molecular electrostatic potential (MEP) maps. The HOMO-LUMO energy gap is a critical descriptor of chemical reactivity and stability. A lower energy gap indicates higher chemical reactivity and improved ability to interact with biological targets. Notably, compound **19** exhibited the lowest HOMO-LUMO gap ($\Delta E = 3.74$ eV), which is consistent with its highest binding affinity in molecular docking ($\Delta G = -8.46$ kcal/mol). This correlation suggests that the electronic softness of compound **19** enhances its adaptability to the EGFR binding pocket, facilitating stronger molecular interactions.

MEP surface analysis revealed regions of negative electrostatic potential primarily around electron-rich atoms such as oxygen and nitrogen, which are potential hydrogen bond acceptors. These regions were aligned with key interaction sites in docking, particularly for compounds **19** and **20**, supporting the formation of stabilizing hydrogen bonds with residues such as Lys721, Gly772, and Glu780 in the EGFR active site. Furthermore, dipole moment values provided additional insight into molecular polarity and potential solubility. Compounds with higher dipole moments, such as compound **20**, may exhibit better aqueous solubility and enhanced pharmacokinetic properties, reinforcing its potential for further biological development. Overall, the DFT results supported the molecular docking findings by highlighting compounds **19** and **20** as the most electronically favorable for EGFR interaction. These data offer a theoretical explanation for their promising bioactivity and validate their selection as lead compounds for further development.

4. Conclusion

In summary, a novel series of quinazoline-amino acid hybrids was synthesized and thoroughly evaluated for antimicrobial and anticancer activities. The compounds demonstrated moderate to strong antimicrobial efficacy, with compounds **4–6**, **15**, **16**, and **18–20** showing the highest antibacterial and antifungal activities. Notably, compound **6** exhibited significant

antibacterial activity with a 39 mm inhibition zone against *Bacillus subtilis*, while compound **15** showed promising antifungal activity and a notable cytotoxic effect against MCF7 breast cancer cells with an IC₅₀ value of 3.40 µg/mL. The molecular docking studies supported the biological findings, with compound **19** showing the best docking score, further confirming the potential of these compounds as effective antimicrobial agents and anticancer candidates. These results highlight the therapeutic promise of quinazoline–amino acid hybrids and suggest that further exploration of their biological mechanisms and clinical relevance could lead to the development of novel therapeutic agents in the fight against infections and cancer.

In summary, a novel series of quinazoline–amino acid hybrids, including ester (**3**, **4**), hydrazide (**5**, **6**, **13**, **17**), dipeptide (**14**–**16**), and tripeptide (**18**–**20**) derivatives, was synthesized and structurally confirmed by IR, ¹H-NMR, ¹³C-NMR spectroscopy, and elemental analysis. The antimicrobial assessment revealed moderate to strong efficacy across the series, with compounds **4**–**6**, **15**, **16**, and **18**–**20** exhibiting the most potent antibacterial and antifungal properties. Notably, compound **6** exhibited the strongest antibacterial activity, producing a 39 mm inhibition zone against *Bacillus subtilis* (MIC = 8 µM, IC₅₀ = 7 µM) and a 36 mm inhibition zone against *Escherichia coli* (MIC = 11 µM, IC₅₀ = 9 µM). Compound **4** also showed strong activity against *E. coli*, with a 33 mm inhibition zone (MIC = 13 µM, IC₅₀ = 11 µM). In terms of antifungal activity, compound **16** demonstrated notable inhibition against *Candida albicans* (13 mm, MIC = 35 µM, IC₅₀ = 28 µM). Molecular docking studies supported the biological data, with compound **19** achieving the highest binding affinity (ΔG = –8.46 kcal/mol), closely matching the reference drug erlotinib (ΔG = –8.51 kcal/mol). Additionally, in vitro anticancer evaluation against MCF7 breast cancer cells revealed that compound **15** had a significant cytotoxic effect with an IC₅₀ of 3.40 ± 0.13 µg/mL, comparable to the standard doxorubicin (IC₅₀ = 2.97 ± 0.12 µg/mL). These results highlight the therapeutic promise of quinazoline–amino acid hybrids and suggest that further exploration of their biological mechanisms and clinical relevance could lead to the development of novel therapeutic agents in the fight against infections and cancer.

5. Conflicts of interest

There is no conflict of interest.

6. Funding sources

This study is supported by the Alexander von Humboldt-Research Fellowship.

7. Acknowledgements

This study was supported by the Alexander von Humboldt Research Fellowship. A. A.-H. A.-R. expresses gratitude for the generous support of the Alexander von Humboldt Foundation.

8. References

- [1] S. Łukasiewicz, M. Czezelewski, A. Forma, J. Baj, R. Sitarz, A. Stanisławek, Breast Cancer-Epidemiology, Risk Factors, Classification, Prognostic Markers, and Current Treatment Strategies-An Updated Review, *Cancers (Basel)*, 13 (2021) 4287. <https://doi.org/10.3390/cancers13174287>.
- [2] R. Baskar, K.A. Lee, R. Yeo, K.W. Yeoh, Cancer and radiation therapy: current advances and future directions, *Int J Med Sci*, 9 (2012) 193–199. <https://doi.org/10.7150/ijms.3635>.
- [3] C. Biray Avci, B. Goker Bagca, M. Nikanfar, L.S. Takanlou, M.S. Takanlou, A. Nourazarian, Tumor microenvironment and cancer metastasis: molecular mechanisms and therapeutic implications, *Front Pharmacol*, 15 (2024) 1442888. <https://doi.org/10.3389/fphar.2024.1442888>.
- [4] N. Zhang, Y. Li, Receptor tyrosine kinases: biological functions and anticancer targeted therapy, *MedComm* (2020), 4 (2023) e446. <https://doi.org/10.1002/mco2.446>.
- [5] C. Pottier, M. Fresnais, M. Gilon, G. Jérusalem, R. Longuespée, N.E. Sounni, Tyrosine kinase inhibitors in cancer: breakthrough and challenges of targeted therapy, *Cancers*, 12 (2020) 731. <https://doi.org/10.3390/cancers12030731>.
- [6] S. Ravez, O. Castillo-Aguilera, P. Depreux, L. Goossens, Quinazoline derivatives as anticancer drugs: a patent review (2011–present), *Expert Opin Ther Pat*, 25 (2015) 789–804. <https://doi.org/10.1517/13543776.2015.1039512>.
- [7] M.R. Waarts, A.J. Stonestrom, Y.C. Park, R.L. Levine, Targeting mutations in cancer, *J Clin Invest*, 132 (2022) e154943. <https://doi.org/10.1172/JCI154943>.
- [8] Y.J. Yu-Jing, C.M. Zhang, Z.P. Liu, Recent developments of small molecule EGFR inhibitors based on the quinazoline core scaffolds, *Anti-Cancer Agents Med Chem*, 12 (2012) 391–406. <https://doi.org/10.2174/187152012800228652>.
- [9] A. Şandor, I. Ionuţ, G. Marc, I. Oniga, D. Eniu, O. Oniga, Structure-Activity Relationship Studies Based on Quinazoline Derivatives as EGFR Kinase Inhibitors (2017–Present), *Pharmaceuticals (Basel)*, 16 (2023) 534. <https://doi.org/10.3390/ph16040534>.
- [10] K.N. Ganjoo, H. Wakelee, Review of erlotinib in the treatment of advanced non-small cell lung cancer, *Biologics*, 1 (2007) 335–346. <https://doi.org/10.2147/btt.s12160296>.
- [11] R.T. Dunto, G.M. Keating, Afatinib: first global approval, *Drugs*, 73 (2013) 1503–1515. <https://doi.org/10.1007/s40265-013-0111-6>.
- [12] G.M. Higa, J. Abraham, Lapatinib in the treatment of breast cancer, *Expert Rev. Anticancer Ther.*, 7(9) (2007) 1183–1192. <https://doi.org/10.1586/14737140.7.9.1183>.
- [13] R. Rosell, E. Carcereny, R. Gervais, A. Vergnenegre, B. Massuti, E. Felip, L. Paz-Ares, Erlotinib versus standard chemotherapy as first-line treatment for European patients with advanced EGFR mutation-positive non-small-cell lung

- cancer (EORTC): a multicentre, open-label, randomised phase 3 trial, *Lancet Oncol.*, 13(3) (2012) 239–246, [https://doi.org/10.1016/S1470-2045\(11\)70393-X](https://doi.org/10.1016/S1470-2045(11)70393-X).
- [14] R. Venkatesh, M.J. Ramaiah, H.K. Gaikwad, S. Janardhan, R. Bantu, L. Nagarapu, M. Bhadra, Luotonin-A based quinazolines cause apoptosis and senescence via HDAC inhibition and activation of tumor suppressor proteins in HeLa cells, *Eur. J. Med. Chem.*, 94 (2015) 87–101, <https://doi.org/10.1016/j.ejmech.2015.02.057>.
- [15] K.K. Vasu, H.D. Ingawale, S.R. Sagar, J.A. Sharma, D.H. Pandya, M. Agarwal, 2-((1H-1,2,3-triazol-1-yl)methyl)-3-phenylquinazolin-4(3H)-ones: Design, synthesis and evaluation as anti-cancer agents, *Curr. Bioact. Compd.*, 14(3) (2018) 254–263, <https://doi.org/10.2174/1573407213666170329131557>.
- [16] H.Q. Zhang, F.H. Gong, J.Q. Ye, C. Zhang, X.H. Yue, C.G. Li, Y.G. Xu, L.P. Sun, Design and discovery of 4-anilinoquinazoline-urea derivatives as dual TK inhibitors of EGFR and VEGFR-2, *Eur. J. Med. Chem.*, 125 (2017) 245–254.
- [17] M.M. Ghorab, A.M. Soliman, K. El-Adl, N.S. Hanafy, New quinazoline sulfonamide derivatives as potential anticancer agents: Identifying a promising hit with dual EGFR/VEGFR-2 inhibitory and radiosensitizing activity, *Bioorg. Chem.*, 140 (2023) 106791.
- [18] M. El-Zahabi, Review on the significance of quinazoline derivatives as broad spectrum anti-cancer agents, *Al-Azhar J. Pharm. Sci.*, (2021), <https://doi.org/10.21608/AJPS.2021.187748>.
- [19] X.F. Shang, S.L. Morris-Natschke, Y.Q. Liu, X. Guo, X.S. Xu, M. Goto, J.C. Li, G.Z. Yang, K.H. Lee, Biologically active quinoline and quinazoline alkaloids part I, *Med. Res. Rev.*, 38(3) (2018) 775–828, <https://doi.org/10.1002/med.21466>.
- [20] R. Karan, P. Agarwal, M. Sinha, N. Mahato, Recent advances on quinazoline derivatives: A potential bioactive scaffold in medicinal chemistry, *ChemEngineering*, 5(4) (2021) 73, <https://doi.org/10.3390/chemengineering5040073>.
- [21] R. Gnanavelou, M. Jayaraman, J. Jayaraman, K.R. Girija, Computational design and structural insights into quinazoline-based lead molecules for targeting PARP10 in cancer therapy, *J. Mol. Graph. Model.*, 137 (2025) 109005, <https://doi.org/10.1016/j.jmgm.2025.109005>.
- [22] A. Dhiman, R. Sharma, R.K. Singh, Target-based anticancer indole derivatives and insight into structure–activity relationship: A mechanistic review update (2018–2021), *Acta Pharm. Sin. B*, 12(7) (2022) 3006–3027, <https://doi.org/10.1016/j.apsb.2022.03.021>.
- [23] J. Haribabu, V. Gariseti, R.E. Malekshah, S. Srividya, D. Gayathri, N. Bhuvanesh, R.V. Mangalaraja, C. Echeverria, R. Karvembu, Design and synthesis of heterocyclic azole-based bioactive compounds: Molecular structures, quantum simulation, and mechanistic studies through docking as multi-target inhibitors of SARS-CoV-2 and cytotoxicity, *J. Mol. Struct.*, 1250 (2022) 131782, <https://doi.org/10.1016/j.molstruc.2021.131782>.
- [24] A.A. Gomaa, A.M. Zeid, I.M. Nagy, The role of genetic polymorphisms in KCNN2 in cardiovascular complications in patients with renal failure, *Gene*, 944 (2025) 149269, <https://doi.org/10.1016/j.gene.2025.149269>.
- [25] A.A.E. Gomaa, A.M.A. Zeid, I.M. Nagy, A.M. Zahran, STIM1 and ORAI1 polymorphisms and erythropoietin resistance in Egyptian ESRD patients, *Clin. Chim. Acta*, 564 (2024) 119948, <https://doi.org/10.1016/j.cca.2024.119948>.
- [26] A.A. Gomaa, A.M. Zeid, I.M. Nagy, The role of GLP1R gene polymorphism in diabetic nephropathy in patients with type 2 diabetes, *Gene Rep.*, 39 (2025) 102205, <https://doi.org/10.1016/j.genrep.2025.102205>.
- [27] H. Yu, Z. Hou, X. Yang, Y. Mou, C. Guo, Design, synthesis, and mechanism of dihydroartemisinin-coumarin hybrids as potential anti-neuroinflammatory agents, *Molecules*, 24 (2019) 1672, <https://doi.org/10.3390/molecules24091672>.
- [28] H.W. Querfurth, F.M. Laferla, Alzheimer's disease, *N. Engl. J. Med.*, 4 (2010) 329–344.
- [29] M.X. Song, X.Q. Deng, Recent development on triazole nucleus in anticonvulsant compounds: a review, *J. Enzyme Inhib. Med. Chem.*, 1 (2018) 453–478.
- [30] C.X. Wei, M. Bian, G.H. Gong, Current research on antiepileptic compounds, *Molecules*, 11 (2015) 20471–20776.
- [31] M. Greaves, Pharmacogenetics in the management of coumarin anticoagulant therapy: the way forward or an expensive diversion?, *PLoS Med.*, 10 (2005) e342.
- [32] A.S. El-Etrawy, A. Ramadan, F.F. Sherbiny, I.F. Zeid, A.A.-H. Abdel-Rahman, M.A. Hawata, Coumarin-amino acid hybrids as promising anticancer agents: design, synthesis, docking studies and CK2 inhibition, *RSC Adv.*, 14 (2024) 24671–24686.
- [33] W. El-Sayed, N. Fathi, A. Gad, E.H. El-Ashry, Synthesis and antiviral evaluation of some 5-N-arylaminoethyl-2-glycosylsulphonyl-1,3,4-oxadiazoles and their analogs against hepatitis A and herpes simplex viruses, *Carbohydr. Chem.*, 27 (2008) 357–372, <https://doi.org/10.1080/07328300802262778>.
- [34] W. El-Sayed, M. Ramiz, A.A.-H. Abdel-Rahman, C-Furyl glycosides, I: synthesis and antimicrobial evaluation of C-furyl glycosides and chalcones derived therefrom, *Monatsh. Chem.*, 139 (2008) 1499–1505, <https://doi.org/10.1007/s00706-008-0941-1>.
- [35] W. El-Sayed, A. Rashad, S. Awad, M. Ali, Synthesis and in vitro antitumor activity of new substituted thiopyrimidine acyclic nucleosides and their thioglycoside analogs, *Nucleosides Nucleotides Nucleic Acids*, 4 (2009) 261–274, <https://doi.org/10.1080/15257770902946165>.
- [36] W. El-Sayed, I.F. Nasser, A.A.-H. Abdel-Rahman, C-Furyl glycosides, II: synthesis and antimicrobial evaluation of C-furyl glycosides bearing pyrazolines, isoxazolines, and 5,6-dihydropyrimidine-2(1H)-thiones, *Monatsh. Chem.*, 140 (2009) 365–370, <https://doi.org/10.1007/s00706-008-0033-2>.
- [37] W. El-Sayed, M. Mahmoud, M. Ramiz, A.A.-H. Abdel-Rahman, Anti-hepatitis B virus activity of new N4-β-D-glycoside pyrazolo[3,4-d]pyrimidine derivatives, *Z. Naturforsch. C*, 64 (2009) 323–328, <https://doi.org/10.1515/znc-2009-5-603>.

- [38] W. El-Sayed, A.A.-H. Abdel-Rahman, M. Ramiz, Synthesis and antimicrobial activity of new substituted 1,2,4-triazoles and their acyclic C-nucleoside analogues, *Zeitschrift für Naturforschung C*, 65 (2010) 15–21. <https://doi.org/10.1515/znc-2010-1-203>.
- [39] W. El-Sayed, I.F. Nassar, A.A.-H. Abdel-Rahman, Synthesis and antitumor activity of new 1,2,4-triazine and [1,2,4]triazolo[4,3-b][1,2,4]triazine derivatives and their thioglycoside and acyclic C-nucleoside analogs, *Journal of Heterocyclic Chemistry*, 48 (2011) 135–243. <https://doi.org/10.1002/chin.201125173>
- [40] A. Kassem, I. Nasser, M. Abd-Aal, M. Awed, W. El-Sayed, Synthesis and anticancer activity of new (furane-2-yl)-1,3,4-thiadiazolyl)-1,3,4-oxadiazole acyclic sugar derivatives, *Chemical and Pharmaceutical Bulletin*, 67 (2019) 888–895. <https://doi.org/10.1248/cpb.c19-00280>.
- [41] A.I. Khodair, M.A. Alsafi, M.S. Nafie, Synthesis, molecular modeling and anti-cancer evaluation of a series of quinazoline derivatives, *Carbohydrate Research*, 486 (2019) 107832. <https://doi.org/10.1016/j.carres.2019.107832>.
- [42] E.F. Ismail, I.A.I. Ali, W. Fathalla, A.A. Alsheikh, E.S. El Tamney, Synthesis of methyl [3-alkyl-2-(2,4-dioxo-3,4-dihydro-2H-quinazolin-1-yl)-acetamido] alkanoate, *Arkivoc*, 2017 (2017) 104–120. <https://doi.org/10.3998/ark.5550190.0018.409>.
- [43] J. Stamos, M.X. Sliwkowski, C. Eigenbrot, Structure of the epidermal growth factor receptor kinase domain alone and in complex with a 4-anilinoquinazoline inhibitor, *Journal of Biological Chemistry*, 277 (2002) 46265–46272. <https://doi.org/10.1074/jbc.M207135200>.
- [44] B.C. Roberts, R.L. Mancera, Ligand–protein docking with water molecules, *Journal of Chemical Information and Modeling*, 48 (2008) 397–408. <https://doi.org/10.1021/ci700285e>.
- [45] F. Wang, W. Yang, R. Li, Z. Sui, G. Cheng, B. Zhou, Molecular description of pyrimidine-based inhibitors with activity against FAK combining 3D-QSAR analysis, molecular docking and molecular dynamics, *Arabian Journal of Chemistry*, 14 (2021) 103144. <https://doi.org/10.1016/j.arabjc.2021.103144>.
- [46] G.M. Morris, R. Huey, W. Lindstrom, M.F. Sanner, R.K. Belew, D.S. Goodsell, A.J. Olson, AutoDock4 and AutoDockTools4: Automated docking with selective receptor flexibility, *Journal of Computational Chemistry*, 30 (2009) 2785–2791.
- [47] G. Bitencourt-Ferreira, V.O. Pintro, W.F. de Azevedo, Docking with AutoDock4, *Methods in Molecular Biology*, 2053 (2019) 125–137.
- [48] G.A. Ross, Introduction to molecular docking and virtual screening, *Methods in Molecular Biology*, 2053 (2019) 141–156.
- [49] W. Chiangjong, S. Chutipongtanate, S. Hongeng, Anticancer peptide: Physicochemical property, functional aspect and trend in clinical application (Review), *Int. J. Oncol.*, 57 (2020) 678–696. <https://doi.org/10.3892/ijo.2020.5099>.
- [50] A. Castro, M.J. Jerez, C. Gil, F. Calderón, T. Doménech, A. Nueda, A. Martínez, CODES, a novel procedure for ligand-based virtual screening: PDE7 inhibitors as an application example, *Eur. J. Med. Chem.*, 43 (2008) 1349–1359. <https://doi.org/10.1016/j.ejmech.2007.10.027>.
- [51] Y.A. Azev, B.V. Golomolzin, T. Dyulcks, N.A. Klyuev, Y.G. Yatluk, Synthesis, properties, and mass-spectrometric fragmentation of 2-thio derivatives of 3-arylquinazolin-4-ones, *Chem. Heterocycl. Compd.*, 43 (2007) 356–361. <https://doi.org/10.1007/s10593-007-0052-7>.
- [52] T.V. Apostol, M.C. Chifiriuc, C. Draghici, L.I. Socea, L.G. Marutescu, O.T. Olaru, G.M. Nitulescu, E.M. Pahontu, G. Saramet, S.F. Barbuceanu, Synthesis, in silico and in vitro evaluation of antimicrobial and toxicity features of new 4-[(4-chlorophenyl)sulfonyl]benzoic acid derivatives, *Molecules*, 26 (2021) 5107. <https://doi.org/10.3390/molecules26165107>.
- [53] T.J. Hossain, Methods for screening and evaluation of antimicrobial activity: A review of protocols, advantages, and limitations, *Eur. J. Microbiol. Immunol.*, 14 (2024) 97–115. <https://doi.org/10.1556/1886.2024.00035>.
- [54] F.M. Sroor, A.A.F. Soliman, E.M. Youssef, et al., Green, facile synthesis and evaluation of unsymmetrical carbamide derivatives as antimicrobial and anticancer agents with mechanistic insights, *Sci. Rep.*, 14 (2024) 15441. <https://doi.org/10.1038/s41598-024-65308-6>.
- [55] V. Khwaza, B.A. Aderibigbe, Antibacterial activity of selected essential oil components and their derivatives: A review, *Antibiotics*, 14 (2025) 68. <https://doi.org/10.3390/antibiotics14010068>.
- [56] M.M. Alidmat, T.Z. Ning, M. Khairuddean, N.H. Shayazi, N.N.S.N.M. Kamal, M. Muhammad, Synthesis, characterization, cytotoxicity study and docking studies of new fused pyrazoline derivatives derived from bis-chalcones against breast cancer cells, *Egypt. J. Chem.*, 64 (2021) 6901–6911.
- [57] H. Rezaei-Seresht, H. Cheshomi, F. Falanji, F. Movahedi-Motlagh, M. Hashemian, E. Mireskandari, Cytotoxic activity of caffeic acid and gallic acid against MCF-7 human breast cancer cells: An in silico and in vitro study, *Avicenna J. Phytomed.*, 9 (2019) 574–586.
- [58] H. Su, K. Ramkissoon, J. Doolittle, M. Clark, J. Khatun, A. Secrest, M. Wolfgang, M. Giddings, The development of ciprofloxacin resistance in *Pseudomonas aeruginosa* involves multiple response stages and multiple proteins, *Antimicrob. Agents Chemother.*, 54 (2010) 4626–4635. <https://doi.org/10.1128/aac.00762-10>.
- [59] Skehan P., Storeng R. New Colorimetric Cytotoxicity Assay for Anticancer-Drug Screening, *Journal of the National Cancer Institut*, 82 (1990) 1107–1112. <https://doi.org/10.1093/jnci/82.13.1107>.